

AD-A094 803

WASHINGTON STATE UNIV PULLMAN DEPT OF PHYSICS F/G 20/5
INTERACTION OF INTENSE INFRARED LASER BEAMS WITH TRANSPARENT SO-ETC(U)
DEC 80 P BRAUNLICH, G BRYANT, A SCHMID F49620-78-C-0095
AFOSR-TR-81-0030 NL

UNCLASSIFIED

1 of 1
AQ 6
094003

END
DATE
FILMED
3-81
DTIC

AFOSR-TR. 81-0030

LEVEL

11

DTIC
ELECTED
FEB 10 1981
C

AD A094803

DDC FILE COPY

Approved for public release;
distribution unlimited.

015

81 2 09 033

REPORT DOCUMENTATION PAGE

UNCLASSIFIED

CLASSIFIED

BEFORE COMPLETION OF FORM

1. REPORT NUMBER AFOSR-TR- 81 - 0030 AD-A094803		2. GOVT ACQUISITION NO.		3. RECIPIENT'S CATALOG NUMBER	
4. TITLE (and Subtitle) Interactions of Intense Infrared Laser Beams with Transparent Solids			5. TYPE OF REPORT & PERIOD COVERED Final 8/1/78 - 9/30/80		
			6. PERFORMING ORG. REPORT NUMBER		
7. AUTHOR(s) P. Braunlich, G. Bryant, A. Schmid, WSU P. Kelly, NRC, Ottawa, Canada			8. CONTRACT OR GRANT NUMBER(s) F49620-78-C-0095		
9. PERFORMING ORGANIZATION NAME AND ADDRESS Department of Physics Washington State University Pullman, WA 99164			10. PROGRAM ELEMENT, PROJECT, TASK AREA & WORK UNIT NUMBERS 61102F 2306/C2		
11. CONTROLLING OFFICE NAME AND ADDRESS Air Force Office of Scientific Research, WFE Building 410 Bolling AFB, Washington, DC 20332			12. REPORT DATE DECEMBER 1, 1980		
			13. NUMBER OF PAGES 71		
14. MONITORING AGENCY NAME & ADDRESS (if different from Controlling Office)			15. SECURITY CLASS. (of this report) unclassified		
			15a. DECLASSIFICATION/DOWNGRADING SCHEDULE		
16. DISTRIBUTION STATEMENT (of this Report) Approved for public release; distribution unlimited.					
17. DISTRIBUTION STATEMENT (of the abstract entered in Block 20, if different from Report)					
18. SUPPLEMENTARY NOTES					
19. KEY WORDS (Continue on reverse side if necessary and identify by block number) Multi-Photon Absorption Laser Beam Deformation Free Carrier Absorption Photon Trajectory Simulation Dielectric Function Aberration Self-Focusing Laser Damage Self-Defocusing NaCl, Ge					
20. ABSTRACT (Continue on reverse side if necessary and identify by block number) In order to investigate beam deformation and depletion at very high photon fluxes, a computational procedure has been developed that is suitable to simulate the propagation of intense beams through transparent solids. It was applied to NaCl exposed to a FWHM 21 psec pulse from a frequency-doubled Nd-YAG laser ($\lambda = 0.532 \mu\text{m}$). The energy content of this TEM ₀₀ -mode pulse is equal to the					

UNCLASSIFIED

SECURITY CLASSIFICATION OF ABSTRACT

experimentally determined single-shot damage threshold of this material. The most convenient mode of data display was found to be a motion picture showing the propagation of the pulse, represented as a colored contour map of the local photon flux, through the focal region. Similar displays of the spatio-temporal development of the free carrier concentration have been made. The material-laser photon interactions in these calculations were based on the two main laser damage mechanisms: avalanche ionization and multiphoton-polaron absorption. The most significant result of these investigations is that, according to both models, beam deformation prevents the build-up of a sufficient photon flux in the interaction area to cause damage at this pulse energy. This means that either both damage mechanisms do not explain the best experimentally available data or these data are extrinsic rather than intrinsic features of the material.

Spherical aberration of the focusing lens as a possible cause for the laser damage morphology observed at threshold in NaCl has been discussed as well. Independently, the response of single-crystalline germanium exposed to intense pulses of 0.45 eV photons was theoretically studied. Quantitative calculations of the relevant multi-photon cross section for free carrier generation and of the dielectric response function have been performed. These results have been coupled with a model, taken from the literature, which describes the resulting changes in the energy distribution of the electrons, holes and both acoustical and optical phonons. These studies represent the first detailed theoretical calculation of the laser damage threshold of germanium at this photon energy.

(11)

Department of Physics
Washington State University
Pullman, WA 99164

Final Report

Dec 1980

WSU L2

INTERACTION OF INTENSE INFRARED LASER

BEAMS WITH TRANSPARENT SOLIDS

by

P. Braunlich, G. Bryant, A. Schmid and P. Kelly

Prepared for AFOSR

Contract

F49620 78-C-0005 free

AIR FORCE OFFICE OF SCIENTIFIC RESEARCH (AFSC)

NOTICE OF TRANSMITTAL TO DDC

This technical report has been reviewed and is approved for public release IAW AFR 190-12 (7b).
Distribution is unlimited.

A. D. SLATT

Technical Information Officer

Max Swerdlow

Contract Monitor

Contract Period:

August 1, 1978 - September 30, 1980

INTERACTIONS OF INTENSE INFRARED LASER BEAMS
WITH TRANSPARENT SOLIDS

by

P. Braunlich, G. Bryant, A. Schmid and P. Kelly

Abstract

In order to investigate beam deformation and depletion at very high photon fluxes, a computational procedure has been developed that is suitable to simulate the propagation of intense beams through transparent solids. It was applied to NaCl exposed to a FWHM 21 psec pulse from a frequency-doubled Nd-YAG laser ($\lambda = 0.532 \mu\text{m}$). The energy content of this TEM_{00} -mode pulse is equal to the experimentally determined single-shot damage threshold of this material. The most convenient mode of data display was found to be a motion picture showing the propagation of the pulse, represented as a colored contour map of the local photon flux, through the focal region. Similar displays of the spatio-temporal development of the free carrier concentration have been made. The material-laser photon interactions in these calculations were based on the two main laser damage mechanisms: avalanche ionization and multiphoton-polaron absorption. The most significant result of these investigations is that, according to both models, beam deformation prevents the build-up of a sufficient photon flux in the interaction area to cause damage at this pulse energy. This means that either both damage mechanisms do not explain the best experimentally available data or these data are extrinsic rather than intrinsic features of the material.

Spherical aberration of the focusing lens as a possible cause for the laser damage morphology observed at threshold in NaCl has been discussed as well. Independently, the response of single-crystalline germanium

exposed to intense pulses of 0.45 eV photons was theoretically studied. Quantitative calculations of the relevant multi-photon cross section for free carrier generation and of the dielectric response function have been performed. These results have been coupled with a model, taken from the literature, which describes the resulting changes in the energy distribution of the electrons, holes and both acoustical and optical phonons. These studies represent the first detailed theoretical calculation of the laser damage threshold of germanium at this photon energy.

Accession For	
THIS CLASS	<input checked="checked" type="checkbox"/>
CLASS B	<input type="checkbox"/>
Unprocessed	<input type="checkbox"/>
Classification	
By	
Distribution	
Digital Tape Codes	
with no/for	
11 111	

A

TABLE OF CONTENTS

	Page
I. Introduction	1
II. Research Objectives and Approach	4
III. Deformation of Intense Laser Beams Tightly Focused Inside NaCl: A Comparison of the Multiphoton-Polaron and Avalanche Models of Optical Breakdown	8
IV. The Contribution of Spherical Aberration to the Vestige Structure Induced by Laser Damage	18
V. Two-Photon Absorption in Ge: Band Effects	39
VI. Interactions of Intense 2.7 μm Picosecond Laser Pulses with Germanium	47
VII. List of Submitted and Planned Publications	62
VIII. List of Professional Personnel	63
IX. Interactions (Coupling Activities)	64
X. Attachment: Computer Code "PULSE"	A-1

I. INTRODUCTION

Exposure of transparent materials to intense laser beams induces changes of their optical properties (conveniently expressed in terms of the dielectric function $\epsilon(\omega)$). This in turn influences the photon trajectories of any beam whose intensity profile is not uniform. The mutual interaction of the photon field and the solid is very complex. The majority of attempts to calculate the spatio-temporal field distribution in a transparent solid having a field-dependent dielectric function are essentially based on solutions of Maxwell's equations.⁽¹⁾ In these calculations it is commonly assumed that the linear refractive index simply increases by $n_2 E^2$ in the presence of an optical field of rms field strength E . Values for the so-called nonlinear refractive index n_2 are taken from measurements (e.g. Smith⁽²⁾) or independent calculations. The most pronounced effect produced by the term $n_2 E^2$ is self-focusing of laser beams having, e.g., a Gaussian intensity profile (TEM_{00} mode). A characteristic feature of these field theories of beam deformation is a singularity of the field strength in the focal waist. As a result, the distribution of the rms optical field strength cannot be determined in the space behind the focal plane. Attempts to do so invariably violate the law of conservation of energy.⁽³⁾

Little if any work has been done on beam deformation due to the reduction of the refractive index caused by the production of photo carriers in the intense photon field.^(4,5) Multiphoton absorption^(4,5,6) or electron impact ionization⁽²⁾ of lattice constituents are mechanisms for the generation of free carriers. Experimental⁽⁷⁾ as well as theoretical⁽⁸⁾ evidence exists for free carrier concentrations to reach up to 10^{21} cm^{-3} at photon fluxes corresponding to the dielectric breakdown threshold of the solid. It is likely that this negative contribution to the refractive index begins

to dominate $n_2 E^2$ already at concentrations around 10^{17} cm^{-3} or less in alkali halides exposed to short laser pulses of optical frequencies.⁽⁴⁾ This clearly indicates that beam deformation (self-defocusing) via a reduction of the refractive index is quite possibly occurring at power densities well below the laser damage threshold. A better understanding of this phenomenon is clearly called for in view of the fact that, during the operation of high power lasers, power densities approaching and--all too frequently--exceeding the damage threshold of exposed optical materials must routinely be handled. In addition to these largely economical reasons, unknown self-focusing and defocusing effects prevent, for example, the exact measurement of the damage threshold of a transparent solid that is subjected to a short laser pulse. Such experiments are commonly executed by tightly focusing the laser beam into the bulk of the sample. Since it is impossible to directly measure the photon flux in the focal region, it is calculated on the basis of diffraction-limited optics, corrected in first order for self-focusing only.⁽²⁾ Photon-induced beam deformation caused, e.g., by negative contributions to the refractive index, has so far never been considered in any detail in the context of laser damage.⁽⁹⁾ An exception is an interesting piece of information on the importance of beam deformation that was provided by Danileiko, Manenkov and Sidorin⁽¹⁰⁾ who tried to damage Ge at $\lambda = 2.76 \text{ }\mu\text{m}$ and $\lambda = 2.94 \text{ }\mu\text{m}$ with nsec pulses. These workers did not succeed because of, as they speculate, free-carrier induced beam self-defocusing. No specifics were given.

A further aspect of beam deformation are spherical aberrations caused by the focusing optics used in typical laser damage experiments. The peculiar damage morphology observed at damage threshold⁽¹¹⁾ was suspected to be in

part due to this effect. Preliminary calculations by Danileiko et al.⁽¹²⁾ indicated that strong spatial intensity oscillations can occur if lenses with residual spherical aberration are employed. We have performed a detailed study of these effects (see Chapter IV) and concluded that the spacing between the obtained intensity peaks does not correspond to the observed spacing between damage sites in the focal volume along the laser beam axis. Yet, a considerable reduction in the peak photon flux may occur in lenses with slight aberration and, thus, influence interpretation of the damage experiments. It was the goal of the work performed under this contract to contribute toward our knowledge of the interaction of intense laser beams with nominally transparent optical materials. The approach chosen to achieve this is outlined in the following section.

II. RESEARCH OBJECTIVES AND APPROACH

The purpose of the work carried out under this contract was to theoretically study several aspects of the interactions of very intense laser pulses with solids. Emphasis was to be placed on infrared photons and infrared optical materials.

In particular, we have investigated the changes of the dielectric response function due to these interactions and the resulting deformation and attenuation of the laser beam. Aberration effects induced by spherical focusing lenses have been discussed as well.

These goals required to not only consider the temporal (dynamic) characteristics of the photon-solid interactions but also to include their spatial variations. Spherical aberration was studied within the paraxial approximation of the wave equation, excluding any non-linear interaction effects such as self-focusing, in an attempt to interpret the peculiar damage morphology observed in the focal volume of the laser beam at threshold peak flux. The nonlinear aspects of the photon-induced changes of the dielectric function required the adoption and development of a special computer code "PULSE". It became operational in the first contract period (Aug. 1, 1978 - July 31, 1979) and was first tested and refined by simulating the classic experiments by Smith et al.⁽¹¹⁾ who focused a 21 psec FWHM pulse at 0.532 μm into NaCl and determined the damage threshold. A motion picture of this damaging pulse, traversing the focal region of a 2.54 cm focal length lens inside NaCl, was deposited at AFOSR. Since then we have included beam depletion in the code and refined the attainable spatial resolution. We applied it to a comparison of beam deformation as obtained under the above mentioned conditions within the avalanche ionization mechanism⁽²⁾ and the multiphoton-polaron absorption model of laser damage. The results are discussed in Chapter III.

The developed computer code is based on a particle-in all method originally used by DÜdder and Henderson.⁽¹³⁾ It is designed to simulate the complete spatio-temporal behavior of a short, intense pulse that is focused into an optical material, independent of the physical mechanisms responsible for the photon-induced changes in the refractive index and the temperature of the exposed solid. Thus, the code is sufficiently flexible to accommodate any flux, wavelength, material and temperature dependence of the dielectric function, any possible mechanism of electronic excitation of the solid (such as multi-photon photo-carrier generation, avalanche ionization and the like) as well as various conceivable mechanisms for converting energy of the photon field to excited electron and phonon distributions and ultimately, to an increase in the lattice temperature. A description of "PULSE" is given in Attachment A. The procedure used to incorporate beam depletion is discussed in Chapter III.

As stated above the calculations of beam deformation at the wavelength in the visible were performed mainly to test the computer code and to demonstrate the feasibility of the chosen computational approach. Difficulties associated with singularities in the focal waist or with energy conservation, characteristic for the theories based on solving field equations, clearly do not occur in our case. We have, for the first time, simulated the rather dramatic break-up of the laser beam expected under the chosen high-power conditions (the energy content of the pulse simulated corresponds to the so-called single-shot damage threshold which has been shown to be well-defined in NaCl⁽¹¹⁾).

In order to apply the developed computational method to materials and lasers of interest for use in the infrared region of the electromagnetic spectrum, it was necessary to establish the mechanism of photon-induced material modifications for this case. Quantitative information on cross

sections for free carrier generation, photon absorption by free carriers and, most importantly, for the calculation of beam deformation, on the photon-induced changes of the dielectric response function is required. We have approached this problem by initially selecting single-crystalline germanium as a typical infrared optical material that is exposed to an intense beam of 0.45 eV photons. Calculations of the involved multiphoton absorption cross section $\sigma^{(2)}$ (two-photon absorption), as well as of the dielectric function have been performed for this case. They are discussed in Chapters V and VI of this report.

REFERENCES
(Chapters I and II)

1. J. H. Marburger, Prog. Quant. Electr. 4, 35 (1975).
2. W. L. Smith, Optical Engineering 17, 489 (1978).
3. A. Glass, Lawrence Livermore Lab, private communication, June 1979.
4. A. Schmid, P. Kelly, P. Braunlich, Phys. Rev. B 16, 4569 (1977).
5. P. Kelly, A. Schmid, P. Braunlich, Phys. Rev. B 20, 815 (1979).
6. P. Braunlich, A. Schmid, P. Kelly, Appl. Phys. Lett. 26, 150 (1975).
7. D. H. Auston, C. V. Shank, Phys. Rev. Lett. 32, 1120 (1974).
8. P. Braunlich, P. Kelly, J. Appl. Phys. 46, 5205 (1975).
9. E. Yablonovitch, N. Bloembergen, Phys. Rev. Lett. 29, 907 (1972).
10. Yu. K. Danileiko, A. A. Manenkov, A. V. Sidorin, in "Laser Induced Damage in Optical Materials" (A. Glass and A. Guenther, eds.), NBS Special Publication 541 (1978).
11. W. L. Smith, J. H. Bechtel, N. Bloembergen, Phys. Rev. B 12, 706 (1975).
12. Yu. K. Danileiko, T. P. Lebedeva, A. A. Manenkov, A. V. Sidorin, Sov. Phys. JETP 47, 401 (1978).
13. H. D. Düdder, D. B. Henderson, Comp. Phys. Comm. 10, 155 (1975).

III.

DEFORMATION OF INTENSE LASER BEAMS TIGHTLY FOCUSED INSIDE NaCl:
A COMPARISON OF THE MULTIPHOTON-POLARON AND AVALANCHE MODELS OF OPTICAL BREAKDOWN

P. Kelly and D. Ritchie
National Research Council
Ottawa, Canada K1A0S1

and

P. Braunlich, A. Schmid, and G. W. Bryant
Department of Physics
Washington State University
Pullman, Washington 99164

Computer simulations of the interaction of intense picosecond laser pulses ($\lambda = 532$ nm) with NaCl in the focal volume of a 3.54 cm focal length aberration-free lens indicate that severe beam deformation may take place at photon fluxes corresponding to the single-shot damage threshold measured under these experimental conditions. This deformation is the result of a change in the dielectric function which, in turn, is caused by free carriers generated via multiphoton-assisted avalanche ionization and/or multiphoton absorption. Strong self-defocusing prevents local photon fluxes from reaching values required to raise the lattice temperature sufficiently for damage to occur. We conclude that either both the avalanche ionization as well as the multiphoton-polaron absorption mechanisms of laser breakdown are invalid in their present form or that the experimentally determined damage thresholds do not pertain to the intrinsic properties of NaCl.

Key words: Avalanche breakdown; Beam deformation; Beam depletion; Free carrier absorption; Multiphoton absorption; Polaron absorption.

1. Introduction

A build-up of very large free carrier concentrations (10^{18} - 10^{20} cm $^{-3}$) during the interaction of intense laser pulses with wide-gap optical materials is thought to be a prerequisite for damage occurrence according to all models of laser breakdown proposed so far [1,2].¹ Recent reviews of this subject were given by Smith [3] and Brawer [4]. Two basic modes of carrier generation are invoked: avalanche ionization of valence electrons after multiphoton generation of so-called starting electrons [5,6] and multiphoton ionization [1,7].

The changes of the dielectric function

$$\epsilon(\omega) = \epsilon_1 + i\epsilon_2 \quad (1)$$

and the ensuing deformation of Gaussian beams, associated with high carrier densities, have been discussed by Yablonovitch and Bloembergen [5] based on a simple Drude model of conductivity and free carrier absorption, and by Schmid et al. [2] who retain the Drude conductivity term for ϵ_2 and replace the phenomenological free carrier absorption contribution to ϵ_2 by free-electron-acoustic-phonon interaction. Detailed calculations of the spatio-temporal flux distribution in the focal volume of an aberration-free lens in NaCl on the basis of the latter mechanism and on the multiphoton ionization-polaron absorption model of laser damage have been presented by Kelly et al. [8]. Severe beam self-defocusing and even beam break-up was shown to take place due to the free-carrier induced reduction in the refractive index. Beam depletion, assumed to be small, was neglected. These calculations were performed in an attempt to explain the damage morphology observed by Smith and coworkers [9] as a possible consequence of the combined effects of self-focusing via $n_2 E^2$ and self-defocusing. Here n_2 is the nonlinear refractive index and E the rms field strength of the optical photon field.

The characteristic damage vestiges of about 1 μ m diameter and 10 μ m spacing along the beam axis, observed at damage threshold and described in reference [9], could not be simulated by these model calculations, quite possibly due to insufficient spatial resolution. In this connection it is of interest to note that a recent discussion of aberration effects on the flux distribution in the focal volume of short focal length lenses could not account for the damage morphology either [10]. Smith et al. [9] believe that local statistical variations of the density of starting electrons are the reason for the damage microsites. They discount any effects of free carriers on the dielectric function and consider only self-focusing. A calculation by these authors of the spatial temperature distribution, i.e. the crystal volume inside an ellipsoidal isothermature surface $T = T_m$, $T_m = 1074$ K is the melting point of NaCl) and its apparent coincidence with a severely damaged region in the focal volume of the laser beam, is taken as one of several important clues for the validity of the avalanche model of laser breakdown [3]. Nevertheless, in light of earlier discussions of the multiphoton-assisted avalanche model which indicated that the free carrier density may reach 10^{19} cm $^{-3}$ for picosecond pulses at damage threshold [5], a detailed computation of self-defocusing based on the avalanche model was clearly desirable.

We have applied the computer code "FULSE," developed by Kelly et al. [8], to this problem and also recalculated the multiphoton-polaron case, because recent improvements in the code now account fully for beam depletion. Thus, direct comparison of both damage mechanisms is possible. The

¹ Figures in brackets indicate the literature references at the end of this paper.

obtained results are remarkable: neither of the two basic models of laser-induced breakdown predict damage at the experimentally determined threshold because of very pronounced self-defocusing.

2. Models of Optical Breakdown

The details of the avalanche ionization model [3,4,6,9] and the multiphoton-polaron absorption model [2,7] of laser breakdown are available from the literature. Three aspects of the photon interaction with optical materials are considered in these model calculations. They concern the mechanisms of carrier generation and their effects on the dielectric function and on lattice heating.

i) Carrier generation

In NaCl, exposed to 532 nm photons, the density, n_c , of free carriers in the conduction band changes according to

$$\dot{n}_c = \omega_i n_c + j^{(4)} n_v F^4 \quad (2)$$

in the avalanche model. The second term in equation (2) supplies the initial electrons. However, avalanche ionization quickly provides the majority of carriers [9]. Its rate is given by

$$\log \omega_i = 3.58 \log E + 8.62 \quad (3)$$

Here E is the rms electric field strength in units of MV cm^{-1} and ω_i is the avalanche ionization rate in sec^{-1} . Only multiphoton carrier generation is retained in the multiphoton-polaron model. All symbols and parameters used above and from here on are explained in table 1.

ii) Lattice heating

In the avalanche model, lattice heating is obtained from the Drude-type conductivity. The energy absorbed per unit time and volume is

$$c_0 \rho \dot{T} = n_c e^2 \tau E^2 / m (1 + \tau^2 \omega^2) \quad (4)$$

The detailed mechanism by which electrons gain energy from the photon field is often referred to as inverse Bremsstrahlung.

According to Pokatilov and Fomin [11], "dressed" electron (or polaron)-phonon scattering with instantaneous relaxation of the excited carriers back to the lower edge of the conduction band is taken as the mechanism by which energy is gained by the lattice in the multiphoton-polaron model [2,7]. It has a cross section σ_p and yields

$$c_0 \rho \dot{T} = \sigma_p F h \omega \quad (5)$$

Beam depletion is accounted for by subtracting the appropriate number of photons in all processes involving the absorption of photons. While this is straightforward for processes involving $j^{(4)}$ and σ_p , the absorbed number of photons per unit volume of crystal materials in the avalanche ionization process is calculated from the energy gained by the lattice according to equation (4), together with the energy required to produce an increase in n_c during a small time interval which, chosen for computational convenience and the desired numerical accuracy, was $\Delta t = 0.03489$ psec.

iii) The dielectric function

Having independently accounted for absorption as described above, only changes in the refractive index, n , need be considered:

$$n = \frac{1}{4} \left(\epsilon_{II} + \sqrt{\epsilon_{II}^2 + \epsilon_{II}^2} \right)^{1/2} + n_2 E \quad (6)$$

The real and imaginary parts of the dielectric function (eq. 1) are taken from the Drude model or from more accurate calculations of the polaron conductivity in the presence of collisions with acoustic phonons [2]. The self-focusing term $n_2 E^2$ is added phenomenologically. For lack of more precise information, we have simply chosen the Drude expressions for all calculations based on the avalanche model:

$$\epsilon_{II} = n_0^2 (1 - 4e^2 \tau^2 n_c / m n_0^2 (1 + \tau^2 \omega^2))$$

and

$$\epsilon_{II} = 4e^2 n_c / m (1 + \tau^2 \omega^2)$$

The value for the collision time τ is still subject to much debate [4]. We used the most recent one available, stated by Brawer [4] to be $\tau = \frac{1}{1.3} \times 10^{-13}$ sec, because it is also consistent with the choice $\epsilon_{II}^2 = 1$ in [11], made in earlier calculations of multiphoton polaron damage [2,7]. An expression by Gurevich et al. is again taken for σ_p . It is stated in reference 2.

Beam deformation is a consequence of the nonuniform beam profile (e.g., a Gaussian) and photon-induced local changes of the refractive index. The computer code "PULSE" was developed to simulate the complete spatio-temporal behavior of short laser pulses traversing optical materials [3]. It was designed to be applicable for any conceivable initial laser beam profile and beam shape, e.g., focused into the material, material distribution (e.g., uniform or layered, materials with refractive index interfaces, clad optical fibers and coatings on substrates). The particular experimental arrangement simulated in the present work is schematically shown in figure 1. It represents the configuration employed by Smith et al. [9,12] in their studies of the damage thresholds in alkali halides at $\lambda = 532$ nm. The FWHM pulse length is 21 psec.

In the model of the pulse, the energy is carried by 10^4 macroscopic "photons" of 10^{11} photons each whose trajectories are followed through the medium [13]. A Gaussian, clipped at the $1/e^2$ values of the peak flux profile in radial direction and in time, is attributed to the pulse and both, the pulse and the medium, are considered rotationally symmetric. These "photons" are injected into the solid with an appropriate group velocity to mimic refraction on the solid interface and focusing by the external $f = 2.54$ cm lens. In the absence of nonlinear photon-material interaction, the focal spot is located 0.2 cm behind the interface air-hal. Appropriate equation of motion, Snell's law of refraction and changes in group velocity of each "photon" are solved to find the changes in direction, group velocity and total photon content (correction for absorption). Simultaneously, the material rate equations (2-5) are solved to determine index n and temperature T . This is achieved by treating all equations as finite differences equations with a time step Δt . For this purpose the interaction volume is divided into cells forming the grid schematically depicted in figure 2. The cell size used in the present calculation is $\Delta r = 0.9$ μ m in radial direction and $\Delta x = 7$ μ m in the direction of beam propagation along the axis. The time step chosen is $\Delta t = 0.03469$ psec. A total of 30 cells in radial and 100 in x-direction form the grid. Further details of "PULSE" are given in reference 13.

Selected flux distributions obtained from both models are presented in figure 3. They show the passage of a 21 psec pulse through the focal region in NaCl in successive time steps of 200 Δt (see indication on the right side of each picture). The peak rms field strength of this pulse is 12.7 MV/cm which corresponds to the measured damage threshold [9,12]. The numbers on the left side and on the x-axis indicate dimensions in μ m. The "expected" location of the focal spot is at $(F,r) = (2000 \mu\text{m}, 0)$. The direction of the beam is from left to right. The color code for the local photon fluxes is given in table 2. Severe beam deformation, particularly past the plane through F perpendicular to the beam axis, is obvious for both models. Yet, the details are distinctly different. This feature is interesting because it points to possibilities of discriminating between the two models of laser damage. For example, the time-integrated spatial flux distribution in a plane past the focal volume could be measured and compared with calculations.

The spatial distribution of the carrier density n_c at $t = 1200$, $\Delta t = 41.9$ psec after arrival of the pulse at $(F,r) = (1500 \mu\text{m}, 0)$ is shown in figures 4 and 5 and the color code is given in table 1. Clearly, the spatial gradient of the refractive index associated with such a distribution is responsible for the observed beam-scattering away from the center of the focal volume.

The spatio-temporal evolution of the lattice temperature T was monitored as well. Remarkably, it did not increase more than 4K above the initial temperature of 300K at any point in the interaction volume for either one of the two models. Thus, damage believed to be the result of rapid temperature pile-up, approaching the melting point $T_m = 1074$ K, is prevented in the discussed case for which breakdown was observed in the experiment by Smith et al. [9,12]. This may only be explained as follows:

- i) Neither one of the two models of laser damage does account for the measured damage data simulated here, and quite possibly, for all other classic experiments in alkali halides which have been used as the basis for the establishment mainly of the avalanche model, or
- ii) not the intrinsic damage properties of the material have been observed in the experiment performed by Smith et al. [9,12], but some extrinsic feature caused the material to fail in the intense photon field of the laser pulse.

Two avenues of further research have to be pursued to resolve this issue. The first one concerns the improvements of the present models. For example, primary defect formation was shown to drastically influence the kinetics of the processes occurring during the pulse event [4]. In particular, the densities of free carriers required for breakdown to be initiated are of the order of magnitude smaller than those obtained when the photochemical reactions, the role of the defects, are disregarded as was the case in the present investigation. The second one concerns the simulation of improved wide gap materials and the performance of new experiments in an attempt to experimentally observe true intrinsic breakdown phenomena.

Acknowledgment

This work was supported by AFOSR contract number F49620-28-C-0095 and by the National Research Council, Ottawa, Canada.

References

- [1] Bräunlich, P. and Kelly, P. J. Appl. Phys. **46**, 5205 (1975).
- [2] Schmid, A., Kelly, P., and Bräunlich, P., Phys. Rev. B **16**, 4569 (1977).
- [3] Smith, W. L., Optical Engineering **17**, 489 (1978).
- [4] Brawer, G., Phys. Rev. B **20**, 3422 (1979).

- [5] Yablonoivitch, E. and Bloembergen, N., Phys. Rev. Lett. **29**, 907 (1972).
- [6] Bräunlich, P., Schmid, A., and Kelly, P., Appl. Phys. Lett. **26**, 150 (1975).
- [7] Kelly, P., Schmid, A., and Bräunlich, P., Phys. Rev. B **20**, 815 (1979).
- [8] Kelly, P., Ritchie, D., Schmid, A., and Bräunlich, P., Proceedings of the 11th Annual Conference on High Laser Power Optical Materials, A. Glass and A. Guenther (ed.), Boulder, Colorado, 1979 (in press).
- [9] Smith, W. L., Bechtel, J. H., and Bloembergen, N., Harvard Technical Report 665 (1976).
- [10] Bryant, G. W. and Schmid, A., Proceedings of the 12th Annual Conference on High Laser Power Optical Materials, A. Glass and A. Guenther (ed.), Boulder, Colorado, 1980 (in press).
- [11] Pokatilov, E. P. and Fomin, V. M., Phys. Stat. Solidi B **73**, 553 (1976).
- [12] Smith, W. C., Bechtel, J. H., and Bloembergen, N., Phys. Rev. B **15**, 4039 (1977).
- [13] Bräunlich, P., Bryant, G., and Kelly, P., Annual Report for Contract AFOSR Number F49620-28-C-0095 (1979).
- [14] Bräunlich, P., Brost, G., Schmid, A., and Kelly, P., Proceedings of the 12th Annual Conference on High Laser Power Optical Materials, A. Glass and A. Guenther (ed.), Boulder, Colorado, 1980 (in press).

Table 1. List of symbols.

n_c	: free carrier density, concentration of electrons in the conduction band [cm^{-3}].
n_v	$= 2.24 \times 10^{22} [\text{cm}^{-3}]$: concentration of valence electrons
ω	: angular frequency of photons
F	: photon flux [number of photons per cm^2 and sec]
λ	$= 532 [\mu\text{m}]$: photon wavelength
E	: rms optical field strength [MV/cm]
μ_i	: avalanche ionization rate [sec^{-1}]
$\sigma^{(4)}$	$= 1.45 \times 10^{-11} [\text{cm}^8 \text{ sec}^{-1}]$ four-photon absorption cross section
σ_p	$= 1.5 \times 10^{-17} [\text{cm}^2]$: polaron absorption cross section
m	$= 0.75 m_e$: mass of free carriers
ρ	$= 2.165 [\text{g cm}^{-3}]$: mass density
c_0	$= 2.0 [\text{cal g}^{-1} \text{K}^{-1}]$: specific heat
T	: temperature [K]
e	: electron charge
τ	$= (1/7.8)10^{-13} \text{sec}$: electron phonon collision time
Δt	$= 0.03489 [\text{psec}]$: time interval used in code "PULSE"
n_0	$= 1.54$ refractive index in the absence of photon-material interactions
n	: refractive index in the presence of photon-material interactions
n_2	$= 6.4 \times 10^{-13} [\text{esu}]$: nonlinear refractive index
ϵ	$= \epsilon_1 + \epsilon_2$: dielectric function

Table 2. Color code for the photon flux [$\text{phot. cm}^{-2} \text{sec}^{-1}$].

$<10^{27}$	Black
10^{27}	White
$10^{27.5}$	Blue
10^{28}	Green
$10^{28.5}$	Red
10^{29}	Yellow
$10^{29.5}$	Magenta
10^{30}	Cyan

Table 3. Color code for carrier density [percent of valence electron density].

$<10^{-5}$	Black
10^{-5}	White
$10^{-4.5}$	Blue
10^{-4}	Green
$10^{-3.5}$	Red
10^{-3}	Yellow
$10^{-2.5}$	Magenta
10^{-2}	Cyan
$10^{-1.5}$	Blue
10^{-1}	Green
$10^{-0.5}$	Red

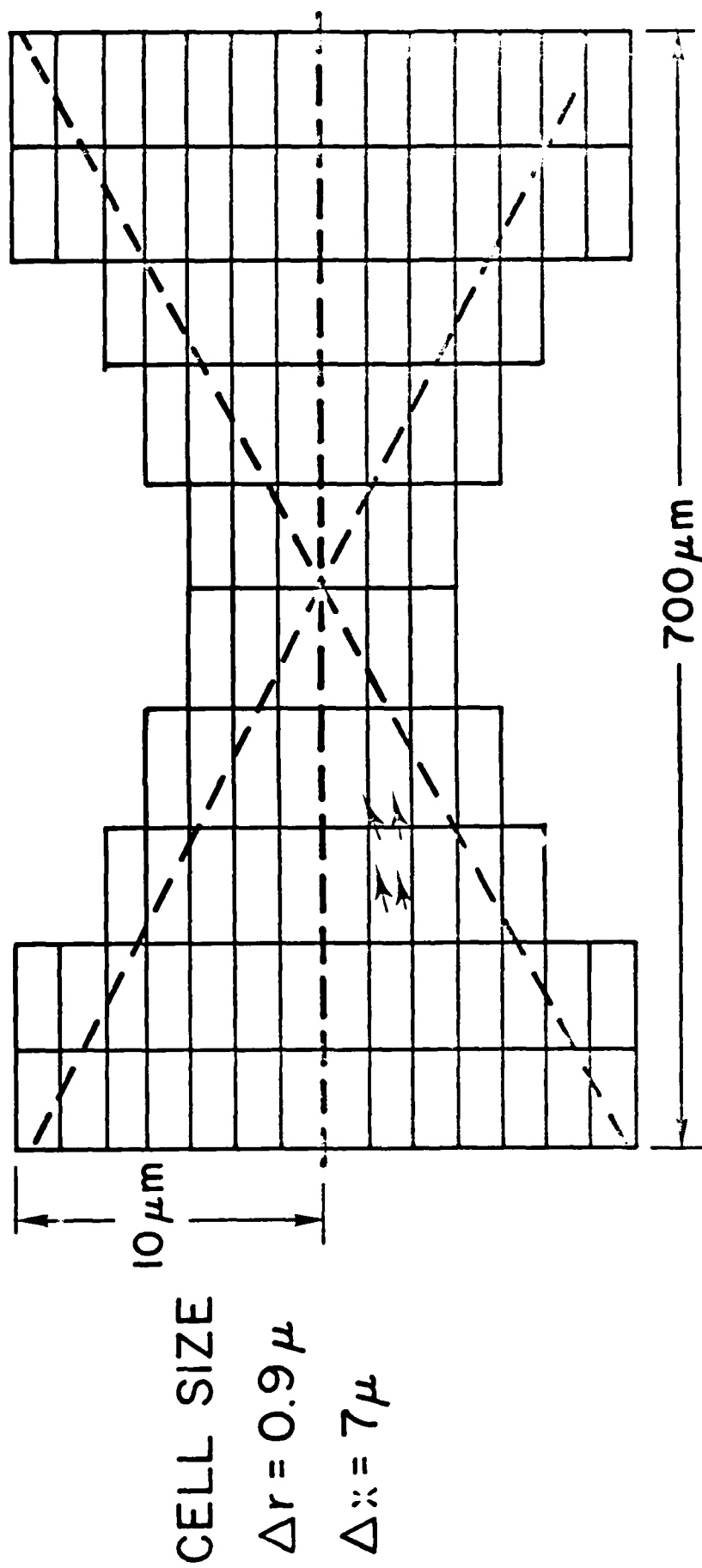


Figure 2. Schematic of the grid geometry used in the computer simulations.

Schematic of Simulated Experimental Arrangement

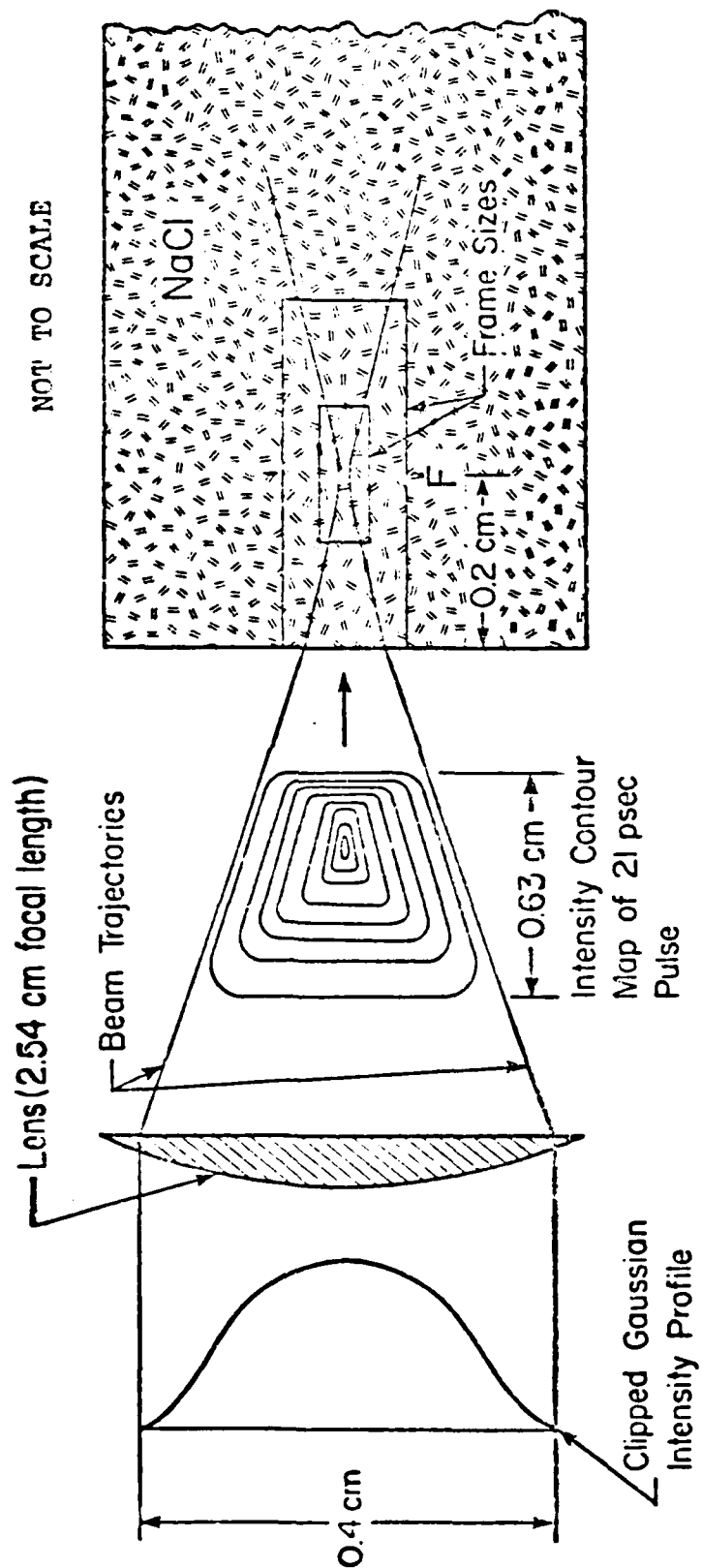


Figure 1. Schematic arrangement of the experiment performed by Smith et al. [9,12].

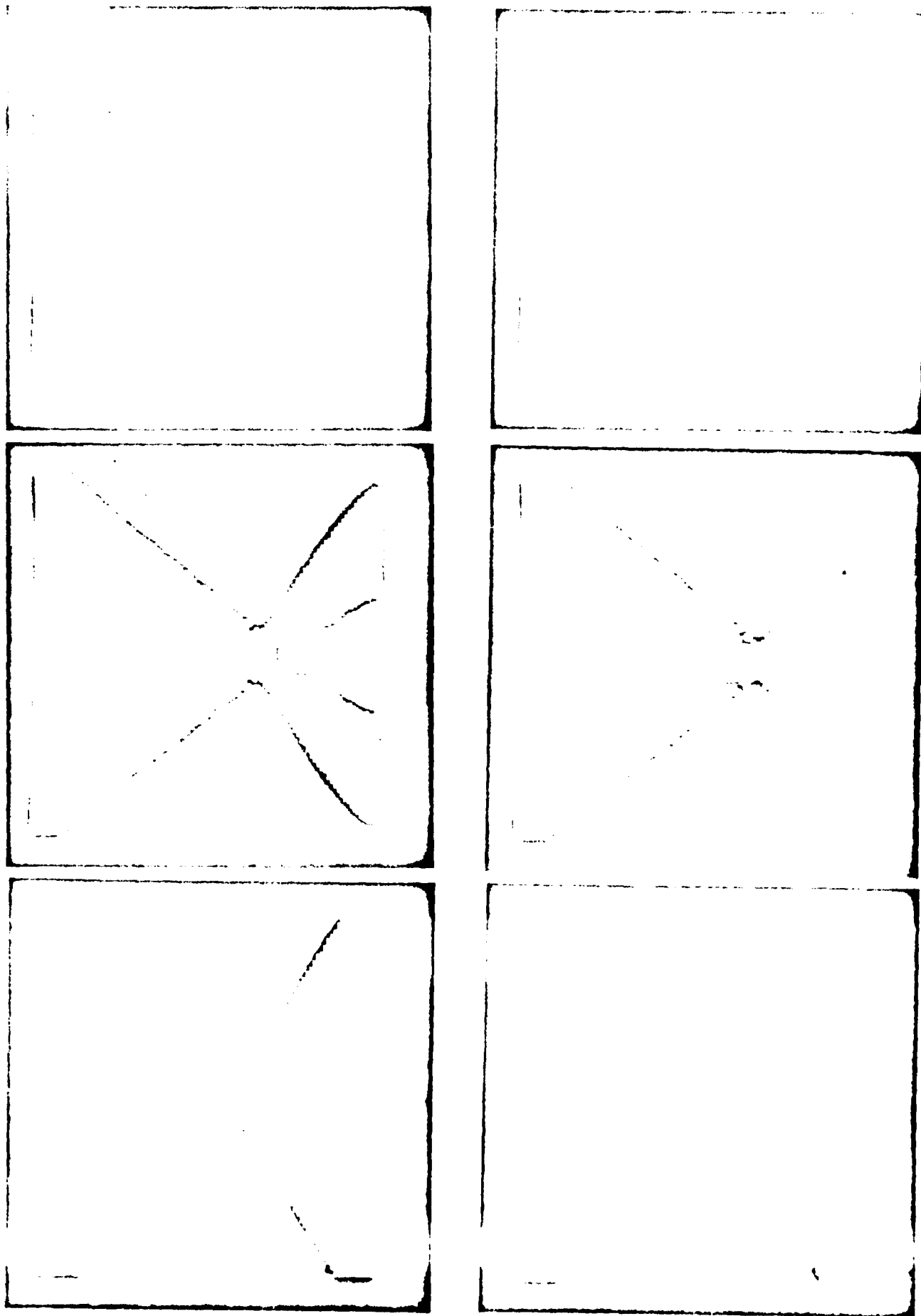


Figure 3

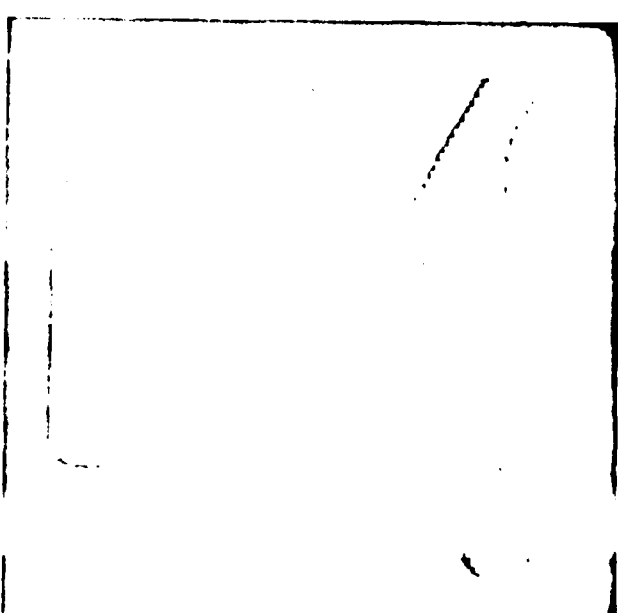
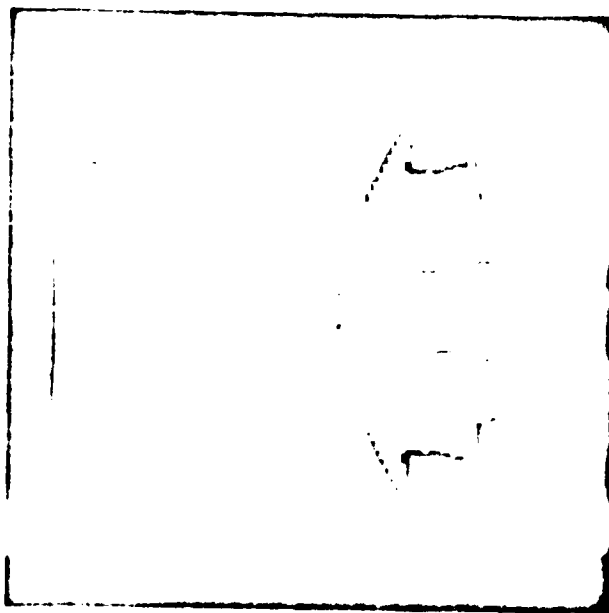
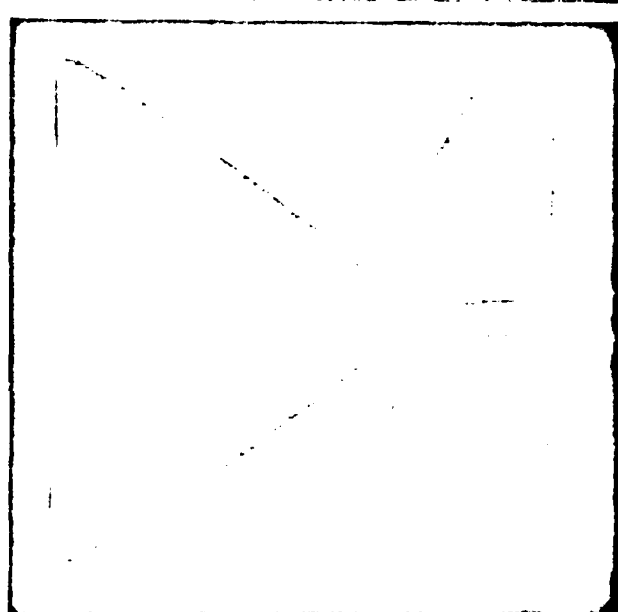
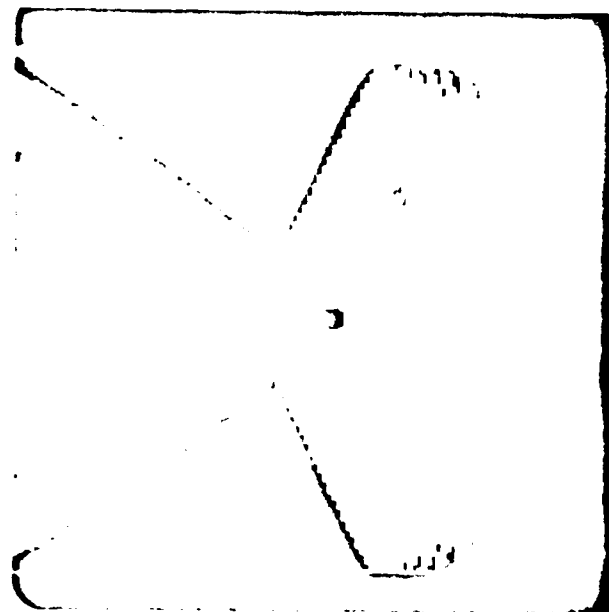
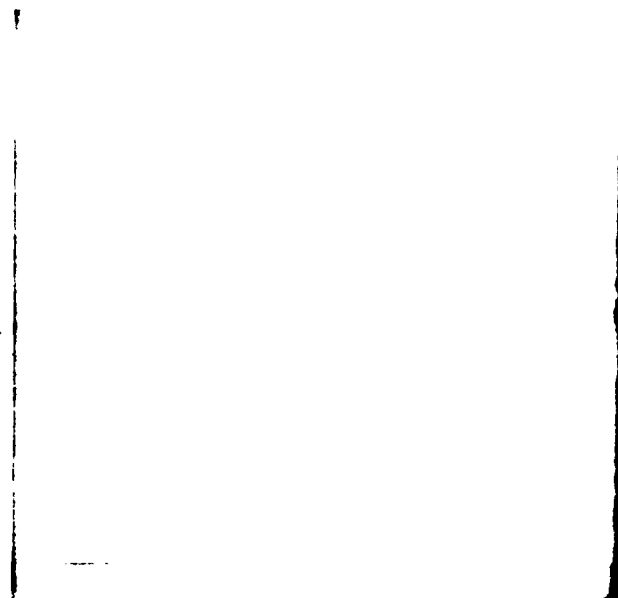
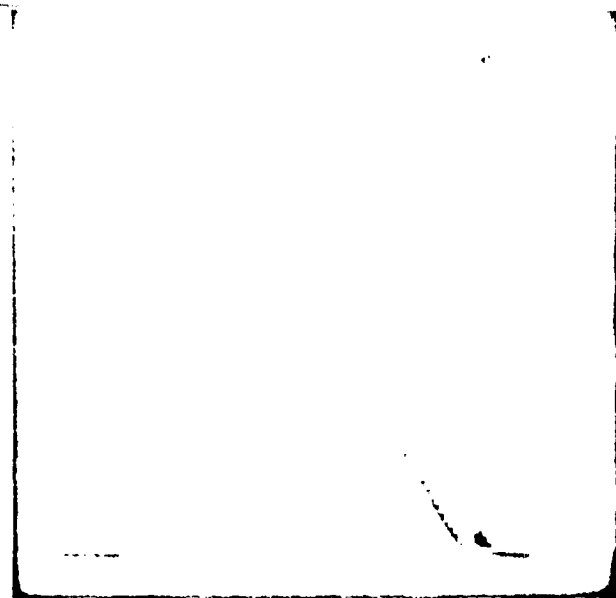


Figure 3 (continued)

Figure 3. Photon flux distributions at various times (in multiples of Δt as indicated at the right of each frame) in the focal volume. The pictures in the left column were obtained from the avalanche model, those in the right column from the multiphoton-polaron model. The color code is given in table 2.

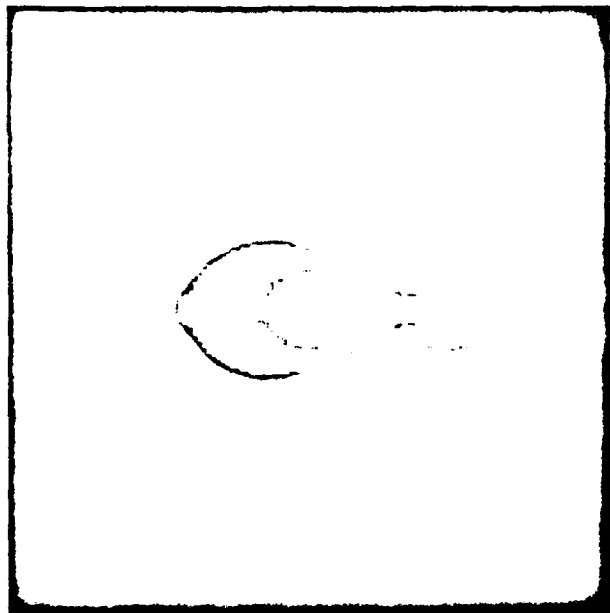


Figure 4. The spatial distribution of the free carrier concentration reached at 4.19 psec = $1200 \times \Delta t$ by avalanche ionization. The color code is given in table 3.

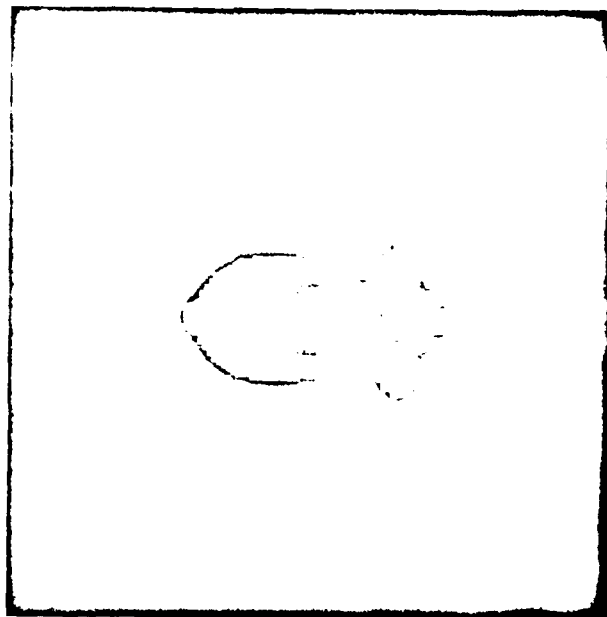


Figure 5. The spatial distribution of the free carrier concentration reached at 41.9 psec by multiphoton ionization. The color code is given in table 3.

IV. The contribution of spherical aberrations to the
vestige structure induced by laser damage

Garnett W. Bryant and Ansgar Schmid

Department of Physics, Washington State University

Pullman, Washington 99164

Abstract

The contribution made to the propagation of a Gaussian pulse by the spherical aberrations introduced by the lens used to focus the beam into the test sample is considered as a possible explanation of the multi-vestige structure observed in laser-induced damage of transparent materials. The paraxial approximation for the wave equation is used to determine the intensity of the pulse on the beam axis when the aberrations are present. The inclusion of spherical aberrations modifies the form expected for a diffraction limited Gaussian beam, shifting the main peak in intensity away from the focus and suppressing it. More importantly, oscillations are introduced in the intensity prior to the focus. Although the spatial arrangement of the peaks in the intensity appears consistent with some of the experimental results for the vestige structure, the spacing between peaks does not correspond to the observed spacing between damage sites. These findings and other possible explanations of the vestige structure are considered critically.

PACS numbers: 42.30.Fk, 42.60.Kg, 61.80-x, 79.20.Ds

I. Introduction

One of the intriguing aspects of recent laser-induced damage studies on wide gap transparent materials is the observation of distinct damage vestiges along the beam axis in addition to the primary damage at the focal spot. Such vestiges have been seen by Danileiko¹ at 2.76μ , by Smith at 1.06μ ² and 0.532μ ³ and by Anthes and Bass⁴ also at 0.532μ . However the observed damage morphology is not the same for all experiments. Using pulses well above the critical power for self-focusing, Danileiko found vestiges separated by roughly 50μ and approximately 10μ in length. This contrasts with Smith's observations, using pulses below the critical power, of 1μ vestiges separated by 10μ . Furthermore, Smith found that the damage sites were statistically spaced around the focal point. In contrast to this Anthes found that all the vestiges occurred prior to the focus.

The avalanche ionization model of breakdown has been used^{2,3} to explain the statistical occurrence of these damage sites. Such an explanation should contradict the findings of Anthes that all the vestiges occurred prior to the focus. However Anthes also used a pulse well above the critical power. As a result, his results would be consistent with Smith's interpretation provided the strong self-focusing present in his experiment selectively enhanced the intensity prior to the focus and suppressed the formation of vestige sites past the focus.

In contrast, Danileiko has recently suggested that spherical aberrations of the Gaussian pulse induced by the lens used to tightly focus the beam into the test material could significantly modify the intensity of the pulse near the focal point, actually shifting the focal point and adding a strong oscillatory modulation to the intensity expected for a diffraction limited, focused Gaussian beam. These strong oscillations in the intensity along the axis

result in regions of enhanced intensity that could cause the vestiges. Previously, such an explanation was used⁵ to successfully explain the appearance and characteristics of damage vestiges in breakdown studies of gases.

Danileiko did not give any details of his calculations of the effects of spherical aberrations. Moreover, he restricted his attention to pulses at 2.76 μ and 10.6 μ . We have performed detailed calculations to extend his results to other wavelengths of interest. In addition we have investigated the effects that variations of the focal length of the focusing lens, the index of refraction of the damaged material, and the position of the lens relative to the sample surface might have on the contributions of the aberrations. We are compelled to consider such variations to compare our results with experimental findings obtained for a variety of situations.

In Section II we describe the calculation of the effect of spherical aberrations on the propagation of a Gaussian pulse. In Section III the results are presented and an approximate expression is derived which predicts the spatial distribution of the regions of enhanced intensity. Finally, in Section IV we relate our results to the observed damage morphology and reconsider the other explanations given for the vestiges.

II. Theory

We use the paraxial approximation to obtain a tractable wave equation for the field $E(\vec{r}, t)$ which includes diffraction of the beam. Specifically, we assume that the field can be written

$$E(\vec{r}, t) = \epsilon(z, \vec{x}_\perp) \exp(i(kz - \omega t)) . \quad (1)$$

ϵ is a slowly varying envelope function, z is the position along the beam axis and \vec{x}_\perp is the position perpendicular to the axis. In the paraxial approximation^{6,7} we solve

$$i \frac{\partial \epsilon}{\partial z} + \frac{1}{2k} \nabla_{\perp}^2 \epsilon = 0, \quad (2)$$

with $k = \omega n/c$ where n is the local index of refraction. The field can be evaluated at any position using known values of the field in one plane ($z = z_p$) perpendicular to the beam axis;⁷ in our case, either at the lens ($z_p = z_L$) or at the sample surface ($z_p = z_S$)

$$\epsilon(z, \vec{x}_{\perp}) = \frac{k}{2\pi i(z-z_p)} \int d^2 x'_{\perp} \exp(ik(\vec{x}'_{\perp} - \vec{x}_{\perp})^2/2(z-z_p)) \epsilon(z_p, \vec{x}'_{\perp}). \quad (3)$$

We consider the typical experimental situation with the lens placed at z_L in free space and the sample surface situated at z_S ($z_S > z_L$). To obtain a description of the field inside the sample ($z > z_S$) we first use Eq. (3) to find $\epsilon(z_S, \vec{x}_{\perp})$,

$$\epsilon(z_S, \vec{x}_{\perp}) = \frac{k_0}{2\pi i(z_S - z_L)} \int d^2 x'_{\perp} \exp(ik_0(\vec{x}'_{\perp} - \vec{x}_{\perp})^2/2(z_S - z_L)) \epsilon(z_L, \vec{x}'_{\perp}) \quad (4)$$

with $k_0 = \omega/c$ in free space. We assume that E is polarized perpendicular to \hat{z} . This of course is not strictly correct. When the initially plane polarized Gaussian beam is focused it obtains a small component of polarization along the beam axis. We ignore this small component. Since E is polarized in the plane of the sample surface, E is continuous across the boundary. Consequently, the field inside the material can be found using Eq. (3) where the known field is at the surface. Thus for $z > z_S$,

$$\epsilon(z, \vec{x}_{\perp}) = \frac{k}{2\pi i(z-z_S)} \int d^2 x'_{\perp} \exp(ik(\vec{x}'_{\perp} - \vec{x}_{\perp})^2/2(z-z_S)) \epsilon(z_S, \vec{x}'_{\perp}) \quad (5)$$

with $k = n\omega/c$ where n is the index of refraction of the sample. Strictly, the continuity of E across the surface implies that

$$\epsilon(z_S + 0^+, \vec{x}_{\perp}) = \exp(i(k_0 - k)z_S) \epsilon(z_S - 0^+, \vec{x}_{\perp})$$

where 0^+ is a positive infinitesimal. The presence of this constant phase factor has no effect on any of the calculations and is ignored.

Using Eq. (3) to evaluate $\epsilon(z, \vec{x}_1)$ we obtain

$$\begin{aligned} \epsilon(z, \vec{x}_1) = & \frac{k k_o}{(2\pi i)^2 (z - z_S)(z_S - z_L)} \int d^2 x'_1 d^2 x''_1 \exp(ik(\vec{x}_1 - \vec{x}'_1)^2 / 2(z - z_S)) \\ & \times \exp(ik_o(\vec{x}'_1 - \vec{x}''_1)^2 / 2(z_S - z_L)) \epsilon(z_L, \vec{x}''_1) . \end{aligned} \quad (6)$$

The integral over \vec{x}'_1 can be performed for $z > z_S$ to yield

$$\epsilon(z, \vec{x}_1) = \frac{k_e}{2\pi i (z - z_L)} \int d^2 x'_1 \exp(ik_e(\vec{x}_1 - \vec{x}'_1)^2 / 2(z - z_L)) \epsilon(z_L, \vec{x}'_1) \quad (7)$$

with

$$k_e = \frac{n k_o (z - z_L)}{n(z_S - z_L) + z - z_S} . \quad (8)$$

This expression for ϵ has the same form as Eq. (3) except that k is replaced by k_e for $z > z_S$.

Note that k_e can be rewritten as

$$\frac{k_e}{z - z_L} = \frac{k_o}{\tilde{z} - z_L} \quad (9)$$

where

$$\tilde{z} = z/n - (1 - n)z_S/n . \quad (10)$$

The only effect of the sample is to change the scale for z inside the sample. The field for $z > z_S$ is the same as that at \tilde{z} in free space provided that z and \tilde{z} are related by Eq. (10). Solving for z we see that $z = n\tilde{z} + (1 - n)z_S$. Thus the length scale spreads by a factor n inside the sample. We are interested in the situation with a focusing lens present. If R_o is the focal length of the lens, then the effective focal length R_g when the sample is present is $R_g + z_L = n(R_o + z_L) + (1 - n)z_S$. Thus

$R_g = R_o + (n-1)(R_o + z_L - z_s)$. The second term is just the shift in the focus obtained using geometrical optics to describe refraction at the surface.

The spherical aberrations introduced by the passage of the beam through the lens are contained in our choice of $\epsilon(z_L, \vec{x}_L)$. Following Born and Wolf⁸ we use

$$\epsilon(z_L, \vec{x}_L) = E_o \exp\left(-\frac{x_L^2}{2a_o^2}\right) \exp\left(-ik_o\left(\frac{x_L^2}{2R_o} + Bx_L^4\right)\right). \quad (11)$$

The first factor in Eq. (11) gives the initial Gaussian profile, the second factor accounts for the distortion of the wave front needed to focus the beam a distance R_o from the lens and the last factor describes the spherical aberrations. For $B > 0$ rays originating off axis are focused more tightly than those near the axis.

We are interested primarily in the intensity of the field on the beam axis. In the paraxial approximation the intensity is given by⁷

$$I = \frac{nc}{8\pi} \{ \hat{z} |\epsilon(z, \vec{x}_L)|^2 + \frac{1}{2ik} (\epsilon^*(z, \vec{x}_L) \vec{\nabla}_L \epsilon(z, \vec{x}_L) - \epsilon(z, \vec{x}_L) \vec{\nabla}_L \epsilon^*(z, \vec{x}_L)) \}. \quad (12)$$

On axis the last term makes no contribution so

$$I(z) = c_s \hat{z} U \quad (12a)$$

where $c_s = c/n$ is the speed of light in the sample and $U = n^2 |\epsilon(z, \vec{x}_L)|^2 / 8\pi$ is the energy density.

Using Eqs. (7) and (11) to evaluate $I(z)$ we obtain

$$I(z) = \frac{cnk_e^2 E_o^2}{32\pi^3 (z-z_L)^2} \int d^2x_1 d^2x_2 \exp\left[\frac{ik_e}{2(z-z_L)} (x_1^2 - x_2^2) - \frac{(x_1^2 + x_2^2)}{2a_o^2} - ik_o\left(\frac{x_1^2 - x_2^2}{2R_o} + B(x_1^4 - x_2^4)\right)\right] \quad (13)$$

Making a change of variables $\vec{u} = \vec{x}_1 + \vec{x}_2$ and $\vec{v} = \vec{x}_1 - \vec{x}_2$, two of the integrations can be performed, yielding

$$I(z) = \frac{cnk_e^2 E_o^2}{32\pi(z-z_L)^2} \int_0^\infty \int_0^\infty uv du dv \exp\left(-\frac{(u^2+v^2)}{4a_o^2}\right) \times J_o\left(\frac{uvk_e}{2(z-z_L)} \left(1 - \frac{z-z_L}{R_e} - B_e(z-z_L)(u^2+v^2)\right)\right) \quad (14)$$

where J_o is a Bessel function, $R_e = R_o k_e / k_o$ and $B_e = Bk_o / k_e$. Letting $u = \rho \cos \theta$ and $v = \rho \sin \theta$, the integral over θ can be done, reducing the expression for I to a single integral

$$I(z) = \frac{cnk_e^2 E_o^2}{16\pi(z-z_L)} \int_0^\infty d\rho \frac{\rho \exp(-\rho^2/4a_o^2) \sin\left(\frac{k_e \rho^2}{4(z-z_L)} \left(1 - \frac{(z-z_L)}{R_e} - (z-z_L)B_e \rho^2\right)\right)}{\left(1 - \frac{(z-z_L)}{R_e} - (z-z_L)B_e \rho^2\right)} \quad (15)$$

This integral, however, can not be done analytically. Consequently, careful numerical evaluations of Eq. (15) to correctly account for the oscillating factor and the pole were performed to determine $I(z)$.

Equation (15) can be derived more directly when no sample is present by using the diffractive ray tracing method of Tappert.⁷ Furthermore, Eq. (15) is analogous to but not equal to the expression used by Evans and Morgan⁵ to study the effect of spherical aberrations on beam propagation in free space. We solve an approximate wave equation exactly. By using the Huygen-Fresnel-Kirchhoff theory of diffraction, Evans and Morgan evaluate approximately an exact integral. Thus it is not clear, a priori, which method gives a better description of the wave propagation. We have not yet made any attempt to compare the two methods. We have however tested the paraxial approximation

calculating corrections to $I(z)$ that go beyond the paraxial approximation by using the field given by Eq. (7). Such corrections change $I(z)$ by no more than a percent and are negligible for our purposes.

All of the beam parameters except B are well known. However, although some of the lenses used in the laser damage experiments are described as well corrected, no explicit values for B are given. As a result, we have performed calculations for a range of values for B . To obtain some feel for the magnitude of B , note that the ray trajectory for the field leaving the lens is given by taking the gradient of the phase of the field. Using Eqs. (1) and (11), we find that the phase is approximately $k_0 z - k_0 x_1^2 / 2R_0 - k_0 B x_1^4$. Thus the ray direction is $k_0 \hat{z} - k_0 (x_1 / R_0 + 4B x_1^3) \hat{x}_1$. The spread Δ along the beam axis between rays originating on axis and rays originating a distance a_0 from the axis at the lens is

$$\Delta = \frac{4Ba_0^2 R_0^2}{1 + 4Ba_0^2 R_0^2} . \quad (16)$$

For Smith's experiment² at 1.06μ the beam radius (at the $1/e$ value) was 0.1 cm and $R_0 = 1.27 \text{ cm}$. Thus Δ is 6μ if $B = 0.01 \text{ cm}^{-3}$ and is 320μ if $B = 0.5 \text{ cm}^{-3}$.

We can make two crude estimates of possible values of B for one of the lenses used by Smith. First, Smith estimated the contribution made by spherical aberrations to the radius of his focal spot in the transverse direction to be 2.6μ . A simple argument using geometrical optics shows that the ratio of transverse spread in spot size to the longitudinal spread due to refraction at the sample surface is $a_0 / 2R_0 n^2$. For NaCl with $a_0 = 0.1 \text{ cm}$ and $R_0 = 1.27 \text{ cm}$ this ratio is $1/60$. If the ratio of transverse to longitudinal spread in spot size due to spherical aberrations is in anyway comparable then $\Delta \approx 160\mu$. This implies a B of 0.25 cm^{-3} .

We can also use expressions given by Born and Wolf⁸ and Ireland⁹ to evaluate B . If we assume that the lens used by Smith was a thin planoconvex lens with a focal length of 1.27 cm then B is about 0.1 cm^{-3} , comparable to the previous estimate. We perform the calculations for B from 0.01 cm^{-3} to 0.5 cm^{-3} . For smaller values of B the spherical aberrations have little effect except when $a_0 \gg 0.1 \text{ cm}$. Moreover larger values of B are probably too big to be reasonable.

III. Results

The results of our calculations for $\lambda = 1.06\mu$ and 0.53μ , $0.01 \text{ cm}^{-3} \leq B \leq 0.1 \text{ cm}^{-3}$ and $0.1 \text{ cm} \leq a_0 \leq 0.3 \text{ cm}$ are shown in Figs. 1-4. In each case the focal length R_0 was 1.27 cm corresponding to the focal length of the lens used by Smith. All intensities are plotted using the same, arbitrary scale proportional to E_0^2 . In addition the results are shown only for propagation through free space. Results for any other combination of focusing lens and sample with $n \neq 1.0$ can be obtained from the present results by using two scaling relations. If we write all distances z in terms of distances Δz from the geometrical focus in the sample, $z = \Delta z + z_L + R_g$, and correspondingly in free space, $\tilde{z} = \Delta \tilde{z} + z_L + R_0$, then Eq. (10) requires that

$$\Delta \tilde{z} = \Delta z / n. \quad (17)$$

Thus for a sample with $n \neq 1.0$ the form of the intensity on the axis is identical to that for propagation through free space provided that distances from the focus are rescaled by n . Note further that, provided the distances Δz are measured from the focal spot, the intensity distribution is independent of the separation between lens and sample.

Furthermore, when $n = 1.0$ the expression for $I(z)$ is

$$I(z) = \frac{ck_o E_o^2}{16\pi(z-z_L)^2} \int_0^\infty d\rho \rho \frac{\exp(-\rho^2/4a_o^2) \sin(\frac{k_o \rho^2}{4} (\frac{1}{z-z_o} - \frac{1}{R_o} - B\rho^2))}{(\frac{1}{z-z_L} - \frac{1}{R_o} - B\rho^2)} \quad (18)$$

When the results for different focusing lenses with focal lengths R_o and R'_o are compared, the intensity at z' in the system with the second lens has the same form as the intensity at z if $1/(z-z_L) - 1/R_o = 1/(z'-z_L) - 1/R'_o$. For small displacements Δz and $\Delta z'$ from the corresponding focal spots $\Delta z' \approx \Delta z R_o'^2/R_o^2$ and the primary effects of a change in R_o are a change in scale of z and a change in scale of I . Thus the results for all R'_o and n can be obtained from one set of calculations for fixed R_o and $n = 1.0$.

Several general features appear when the spherical aberrations are included. First the primary peak in intensity no longer occurs at the geometrical focal spot, but instead occurs prior to it. Moreover, the main peak is smaller when the aberrations are included than it is for the corresponding Gaussian beam, indicating the extra transverse spread of the beam when the aberrations are included. This decrease can be as much as two orders of magnitude when the aberrations are large. When the spherical aberration is sufficiently strong and the beam not too narrow, oscillations occur in the on-axis intensity resulting from constructive and destructive interference. We will consider these oscillations in intensity in Section IV as a possible explanation for the multiple damage sites. The intensity is only shown prior to the focus in the figures. Beyond that point there are no more oscillations in intensity and the intensity approaches that for the diffraction limited Gaussian beam without aberration.

Comparing Figs. 1-4 shows the effect of the beam radius a_o , wavelength λ and aberration B on the pulse propagation. First, as the beam becomes

broadener, the spherical aberration (proportional to x_1^4) becomes more important. For small a_0 the oscillations disappear and the main peak approaches in magnitude the intensity of the Gaussian beam at the focus. For large a_0 the main peak is much smaller relative to the Gaussian focal intensity while the secondary peaks are much larger relative to the main peak. The absolute magnitude of intensity increases for increasing a_0 simply because a broader beam is focused.

When λ is varied the aberrations become more important for smaller λ . This is evident from Eq. (18). Decreasing λ (increasing k_0) is equivalent to simultaneously decreasing R_0 , which compresses the oscillations, and increasing B , which enhances the magnitude of the oscillations. Consequently similar trends occur for decreasing λ that occur for increasing a_0 . The main peak decreases relative to the peak of the Gaussian beam while the side peaks become more important. Although the positions of the secondary peaks are insensitive to changes in a_0 , they are very sensitive to changes in λ . The pattern is compressed for small λ . This also occurs for a Gaussian pulse without aberration. Pulses for smaller λ are much more sharply focused because diffraction is less important.

When B is increased the pattern spreads out and the side peaks become more important. This contrasts with the change that occurs when λ is increased and the pattern spread out but the side peaks become weaker. In all cases, the trends observed for a_0 and B at one wavelength occur at all other wavelengths considered between 0.53μ and 10.6μ . However for very long wavelengths ($\lambda \geq 10.6\mu$) the oscillations are only present for large beams ($a_0 \geq 0.3$ cm) or large aberrations ($B \geq 0.1$ cm⁻³).

One can obtain an approximate relation for the position of the maxima and minima in the intensity by considering Eq. (18). The position of these

extrema are controlled by the zeros of the sine function in Eq. (18). The zeros are given by the solutions of

$$v - cv^2 = m\pi \quad (19)$$

with $v = k_o^2(R_o - z + z_L)/4R_o(z - z_L)$, $c = (z - z_L)^2 R_o^2 4B / (R_o - z + z_L)^2 k_o$ and m an integer. The roots are

$$v = \frac{1 \pm (1 - 4\pi mc)^{1/2}}{2c} \quad (20)$$

Roots are possible for all $m < m_s$ such that $4\pi cm_s < 1 < 4\pi c(m_s + 1)$. When $4\pi c(m_s + 1) = 1$ another zero of the sine function occurs. For z slightly further from the focus ($z - z_L$ smaller) c decreases and $4\pi c(m_s + 1) < 1$. In the region between the new zeros at $v = (1 \pm (1 - 4\pi c(m_s + 1))^{1/2})/2c$, the sine takes on the opposite sign to adjacent regions. Thus if the sine is negative between the two new zeros, a new negative contribution is made to the integral of Eq. (18) and the intensity decreases. Conversely, if the sine is positive between the two new zeros, then the integral will increase. Thus we expect the extrema to occur for z_m that solve $4\pi cm = 1$ ($m > 0$). These are given by

$$z_m = z_L + \left(\frac{k_o}{16\pi B m}\right)^{1/2} / \left(1 + \left(\frac{k_o}{16\pi B R_o^2 m}\right)^{1/2}\right) \quad (21)$$

This is not an exact relation for the positions of the extrema because it does not include the contribution made by the other factors in the integrand.

Equation (21) overestimates the distance between the geometrical focus and an extremum, especially the distance of the main peak from the geometrical focus. Equation (21) gives a much better description of the positions of the secondary peaks. Moreover, since the relative error made for each peak position is similar, Eq. (21) is much more accurate at predicting the separation between

peaks. Note that z_m is independent of a_0 . Inspection of the figures confirms that the peak positions are insensitive to beam width. Ireland⁹ also made a similar observation. Finally, Eq. (21) confirms the numerical calculations that show the peaks nearer to the focus to be farther apart.

IV. Conclusions

Although the contribution of spherical aberrations appears to be important for an understanding of the damage morphology in gases, the results for breakdown in bulk materials are inconclusive. Notice that the spacing between peaks when $\lambda = 1.06\mu$ and $B = 0.01 \text{ cm}^{-3}$ (Fig. 1) is roughly 20μ near the main peak. Moreover this separation must be scaled by the index of refraction ($n = 1.53$ for NaCl). A separation of 30μ is much larger than that observed by Smith.² Furthermore, the separation only gets larger for larger B (Figs. 2 and 3). Similarly the spacing in Fig. 4 for $\lambda = 0.53\mu$ is much larger than that reported by Smith. The spacing observed by Danileiko at 2.76μ is much greater and thus more comparable to our results. However, spherical aberrations are less important at 2.76μ than at 1.06μ or 0.53μ so the better agreement is puzzling.

There are, however, several other interesting features about the observed morphology. Anthes and Bass found no damage sites after the focal spot. They attributed this to a suppression of the intensity in this region due to self-focusing prior to the focal spot. However it is equally possible that no damage sites occur after the focal spot because no oscillations in intensity occur in this region. In addition, in several of the published pictures of damage morphology presented by Smith,^{2,3} the separation between sites increases in the direction of the beam propagation. This structure corresponds to our results that the peaks are farther apart nearer the focus provided all of the sites observed by Smith occurred prior to the focus. It

would be difficult to reconcile such a structure with the random structure predicted by the avalanche model.

Another problem that arises when spherical aberrations are considered is the appearance of so many vestige sites for pulse powers just above threshold. As the figures show, there is a rapid decrease in the magnitudes of the peaks farther from the focus except when B or a_0 is large. However Smith's results were obtained with narrow beams ($a_0 = 0.11 \pm 0.01$ cm). Thus it is not clear how the secondary peaks can cause intrinsic damage if the main peak is just above the threshold intensity.

Although the contribution of spherical aberrations to the damage morphology is not yet compelling, we have not completed consideration of this contribution when self-focusing is included. We expect the self-focusing to selectively enhance the peaks in intensity, greatly magnifying the effect of spherical aberrations. Even if B were chosen sufficiently small to obtain the correct spacing between vestiges, the self-focusing might enhance the secondary peaks sufficiently to cause damage at those sites as well as at the primary peak. We have begun a study to include the self-focusing but no results are available yet.

Several questions still remain. First, even for small aberrations, the main peak is less than the corresponding peak of the Gaussian pulse without aberrations. Such a suppression should affect the interpretation of damage experiments but so far has been ignored. Thus, more careful determination of the spherical aberrations present in experiments should be made and a more accurate descriptions of the beam propagation used. Even in the simplest case when B vanishes the proper description of the beam propagation should be used. Smith used a diffraction limited Gaussian beam with a diffraction length $k_0 a_0^2$ determined from the width of the beam at the focus. That

diffraction length is much shorter than the one we use where a_0 is the radius of the beam at the lens. As a result, the Gaussian beam we use is much sharper near the focus (this is primarily determined by how tight the focus is rather than by the diffraction length) than the pulse used by Smith. Consequently the good success he had in predicting the spatial range over which vestiges could occur would not be possible if our diffraction limited Gaussian pulse were used.

In summary, we find that the contribution of spherical aberrations to be an incomplete explanation for the vestiges. It is unable with a small B to simultaneously explain the observed small spacing between vestiges and the occurrence of so many damage sites. However the spherical aberrations do cause a systematic variation in site distribution which is evident in some experimental results. It is still unclear how important spherical aberrations are and whether self-focusing will enhance their contribution. Unfortunately, the explanation of Smith is also unsatisfactory. Use of the overly broad intensity distribution allows the avalanche model to predict the occurrence of damage spots over a much wider spatial range than is justified. Much work still needs to be done before a complete understanding of the damage morphology is possible.

Acknowledgments: The authors gratefully acknowledge the many useful conversations with P. Braunlich and the support of the Air Force Office of Scientific Research through AFOSR Contract No. F49620-78-C-0095.

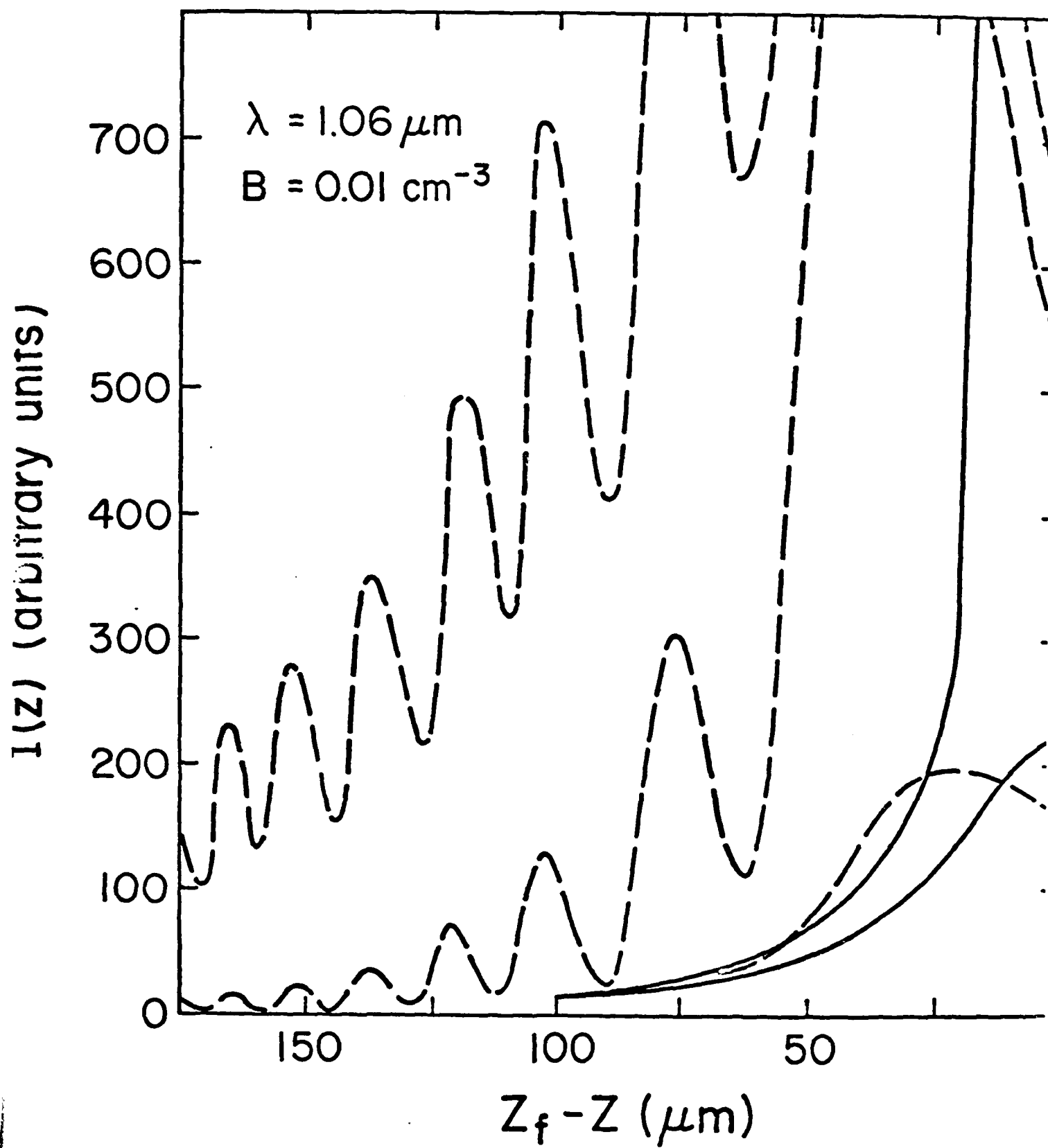
References

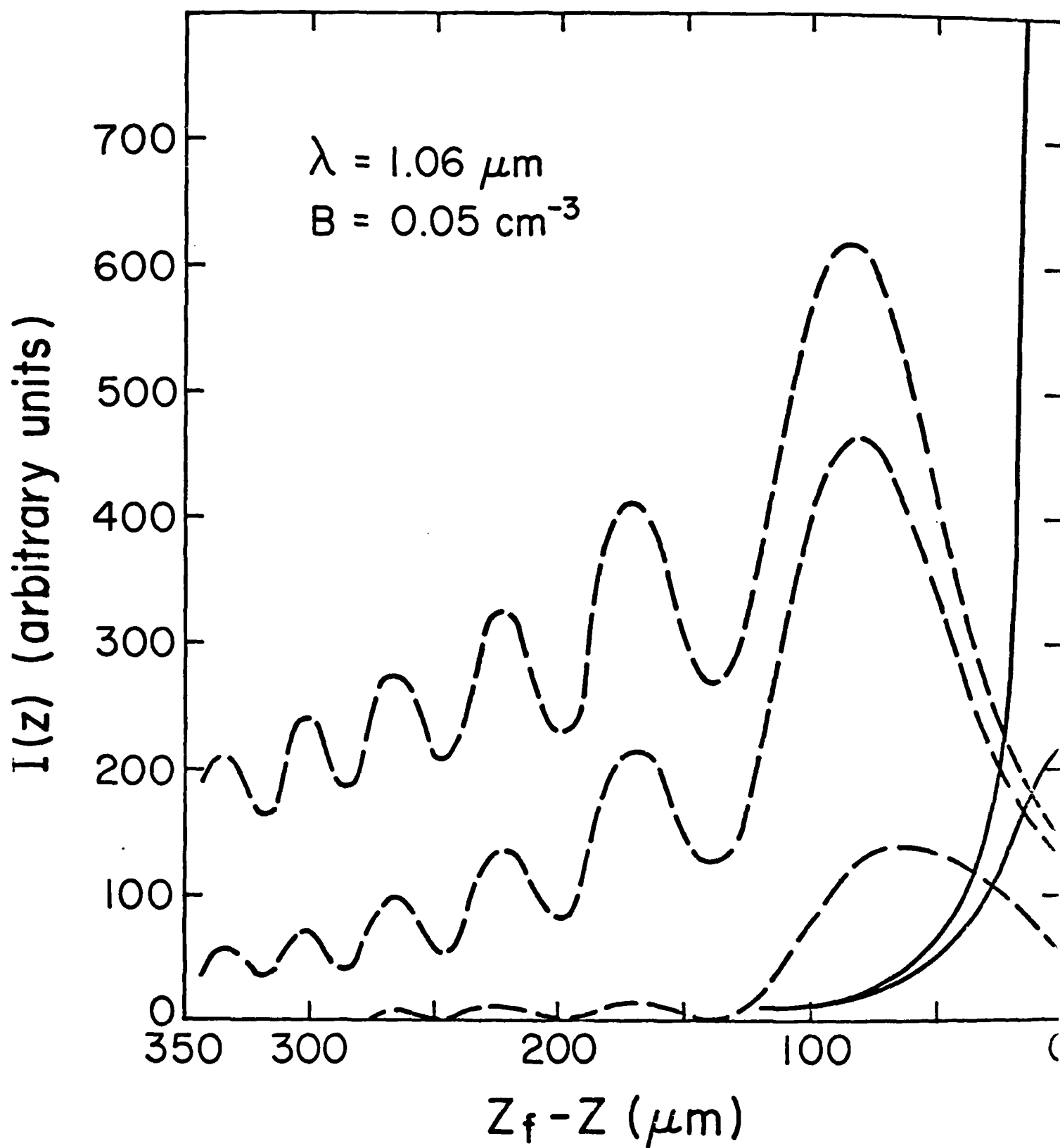
(Chap. IV)

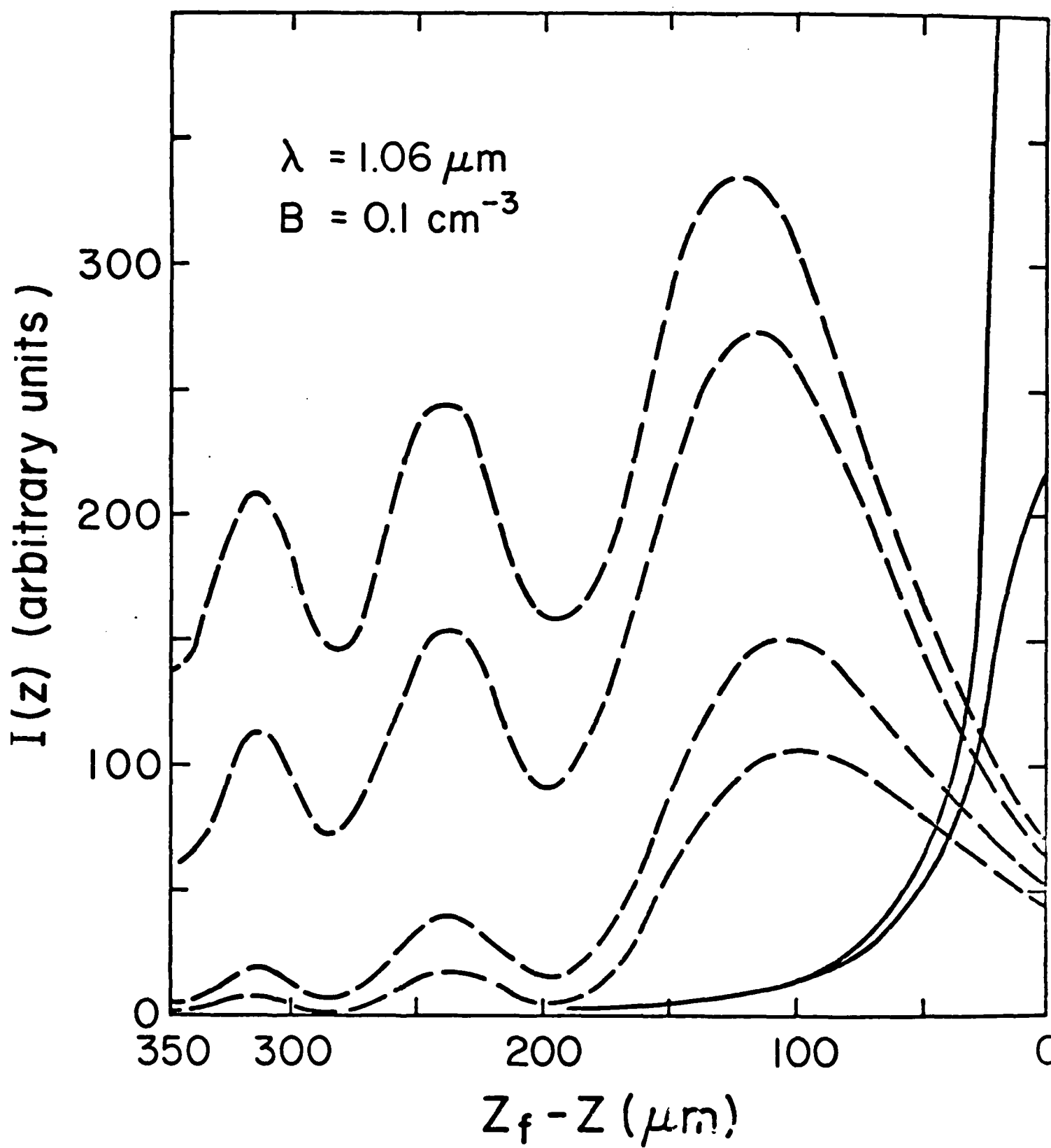
1. Yu. K. Danileiko, T. P. Lebedeva, A. A. Manenkov, and A. V. Sidorin, "Investigation of mechanisms of damage to semiconductors by high-power infrared laser radiation," Zh. Eksp. Teor. Fiz. 74, 765-771 (1978) [Sov. Phys. JETP 47, 401-404 (1978)].
2. W. Lee Smith, J. H. Bechtel, and N. Bloembergen, "Picosecond laser-induced damage morphology: spatially resolved microscopic plasma sites," Opt. Commun. 18, 592-596 (1976).
3. W. Lee Smith, J. H. Bechtel, and N. Bloembergen, "Picosecond laser-induced breakdown at 5321 and 3547 Å: observation of frequency dependent behavior," Phys. Rev. B 15, 4039-4055 (1977).
4. J. P. Anthes and M. Bass, "Direct observation of the dynamics of picosecond-pulse optical breakdown," Appl. Phys. Lett. 31, 412-414 (1977).
5. L. R. Evans and C. Grey Morgan, "Lens aberration effects in optical-frequency breakdown of gases," Phys. Rev. Lett. 22, 1099-1102 (1969).
6. M. Lax, W. H. Louisell, and W. B. McKnight, "From Maxwell to paraxial wave optics," Phys. Rev. A 11, 1365-1370 (1975).
7. F. Tappert, "Diffractive ray tracing of laser beams," J. Opt. Soc. Am. 66, 1368-1373 (1976).
8. M. Born and E. Wolf, Principles of Optics, 4th ed. (Pergamon, Oxford, England, 1975).
9. C. L. M. Ireland, A. Yi, J. M. Aaron, and C. Grey Morgan, "Focal-length dependence of air breakdown by a 20-psec laser pulse," Appl. Phys. Lett. 24, 175-177 (1974).

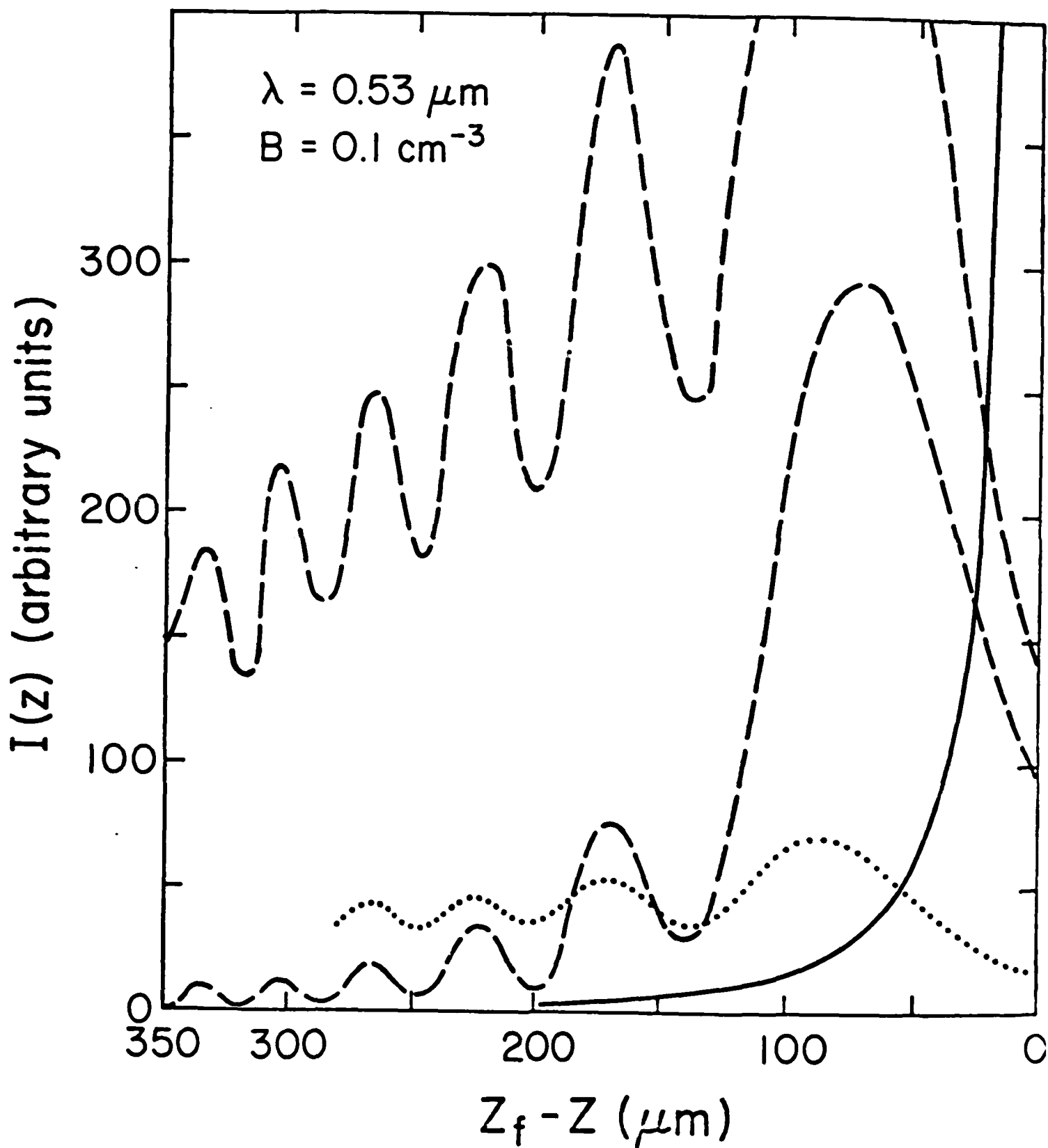
Figure Captions

1. On axis intensity for propagation in free space when $\lambda = 1.06\mu$ and $B = 0.01 \text{ cm}^{-3}$. The region shown is prior to the focus z_f . The solid lines are for Gaussian beams without aberration ($a_0 = 0.1 \text{ cm}$ and 0.3 cm for the lower and upper curves respectively, the maximum intensity when $a_0 = 0.3 \text{ cm}$ is 1.7×10^4). The dashed curves include the aberrations ($a_0 = 0.1 \text{ cm}$, 0.2 cm and 0.3 cm respectively for the curves in order of increasing magnitude, the maximum intensity when $a_0 = 0.2 \text{ cm}$ is 1.3×10^3 and when $a_0 = 0.3 \text{ cm}$ is 2.3×10^3 and 1.1×10^3 for the first two peaks).
2. On axis intensity for propagation in free space when $\lambda = 1.06\mu$ and $B = 0.05 \text{ cm}^{-3}$. The solid lines are for beams without aberration ($a_0 = 0.1 \text{ cm}$ and 0.3 cm for the lower and upper curves respectively). The dashed curves include the aberrations ($a_0 = 0.1 \text{ cm}$, 0.2 cm , and 0.3 cm respectively for the curves in order of increasing magnitude).
3. On axis intensity for propagation in free space when $\lambda = 1.06\mu$ and $B = 0.1 \text{ cm}^{-3}$. The solid lines are for beams without aberration ($a_0 = 0.1 \text{ cm}$ and 0.3 cm for the lower and upper curves respectively). The dashed curves include the aberrations ($a_0 = 0.1 \text{ cm}$, 0.12 cm , 0.2 cm , and 0.3 cm respectively for the curves in order of increasing magnitude).
4. On axis intensity for propagation in free space when $\lambda = 0.53\mu$ and $B = 0.1 \text{ cm}^{-3}$. The solid curve is for a beam without aberration ($a_0 = 0.1 \text{ cm}$). The dashed curves include the aberrations ($a_0 = 0.1 \text{ cm}$ and 0.2 cm respectively for the lower and upper curves, the maximum intensity when $a_0 = 0.2 \text{ cm}$ is 600). The dotted curve includes aberrations when $a_0 = 0.3 \text{ cm}$ and is scaled by 10^{-1} .









Two-photon absorption in Ge: Band effects

Garnett W. Bryant

Department of Physics, Washington State University, Pullman, Washington 99164

(Received 10 January 1980)

Calculations are reported of the two-photon absorption in germanium using a Kane band model. All bands within 10 eV of the valence-band edge are considered. The matrix elements are evaluated using $\mathbf{k}\cdot\mathbf{p}$ theory to find the relevant wave functions. The spherical model of Valdeschi and Lipari is used to treat the distinction between the light-hole and heavy-hole bands properly. Detailed calculations are made to test various approximations that simplify the evaluation of these complicated nonlinear optical coefficients. For Ge it is essential that the split-off band be included as an intermediate state and that the nonparabolicity of the conduction band be treated correctly. The results of the most complete calculation are in good agreement with experimental results.

I. INTRODUCTION

With the advent of high-intensity lasers, the study of multiphoton transitions has become increasingly more important. Because the selection rules for single and multiphoton transitions are different, each provides different information on a material's band structure. Multiphoton transitions also provide another avenue for studying exciton effects. Furthermore, the study of these processes aids in the understanding and description of the propagation of intense electromagnetic fields through nonlinear materials.

In this paper we present a theoretical study of the two-photon absorption in germanium. There are two important reasons for studying Ge. First, the experimental results for Ge are not extensive and those that are available are not consistent. Zubov *et al.*¹ measured the two-photon absorption coefficient K_2 at 2.36 μm and found it to be 1 cm/MW. Wenzel *et al.*² found that K_2 was 2.5 cm/MW near 2.7 μm . This result is inconsistent with the more recent results of Gibson *et al.*³ for the wavelength range from 2.65 to 3.0 μm . They found that K_2 is less than 0.75 cm/MW throughout this region and is only 0.50 cm/MW at 2.7 μm . Gibson *et al.* were one of the first to eliminate the contribution made to the measured total absorption by those carriers generated in the two-photon absorption process. Consequently, they extracted two-photon absorption coefficients that were lower than the previously measured total absorption coefficients. Gibson *et al.* also reanalyzed earlier data^{1,2} for InSb using their more detailed interpretation of the data. Their results were again several orders of magnitude lower than the previous experimental and theoretical estimates. However, more recent results⁴ suggest that Gibson's results for InSb are too low because the conduction electron density of the InSb samples was sufficiently high for electrons to fill the con-

duction-band states needed for the two-photon absorption. We expect this effect to be far less important in Ge with a band gap five times larger than in InSb. Consequently the Gibson results should be the most reliable available for Ge.

The second reason for considering Ge is that it has not been studied theoretically as much as the zinc-blende semiconductors.^{5,7,8} Only Arifzhanov and Ivchenko⁹ have considered Ge in detail. They provided a group-theoretical analysis of the expression for K_2 but gave no explicit results for K_2 . Ge has not been extensively studied for several reasons. For other semiconductors one can often make the approximation that the splitting Δ between the valence and split-off band edges is either much greater or smaller than the energy gap E_g between conduction and valence bands. Such approximations greatly simplify the matrix elements that must be calculated. However, in Ge $\Delta \sim E_g$. Furthermore, for the zinc-blende semiconductors one can choose basis states so that the matrix elements involving states with wave vector \mathbf{k} transform simply when considering states with different wave vectors. Due to the symmetry of the conduction basis states in Ge (they have the symmetry Γ_7^- rather than Γ_6^-) this is not possible. These two complications make the evaluation of matrix elements and the summation over intermediate states more difficult to perform for Ge.

In Sec. II we present the calculations of K_2 . We consider only direct two-photon transitions in Ge. Near threshold a hole is created in the heavy-hole (hh) or light-hole (lh) valence bands and an electron fills a state in the lowest conduction band (c). For higher photon energies we also consider transitions where a hole in the split-off (so) bands is created. Two-photon absorption is a two-step process. We thus consider all transitions where the intermediate state is one of the above states or a state in the next highest conduction band (i.e., the Γ_8^- band). These bands are shown in Fig. 1. In each case,

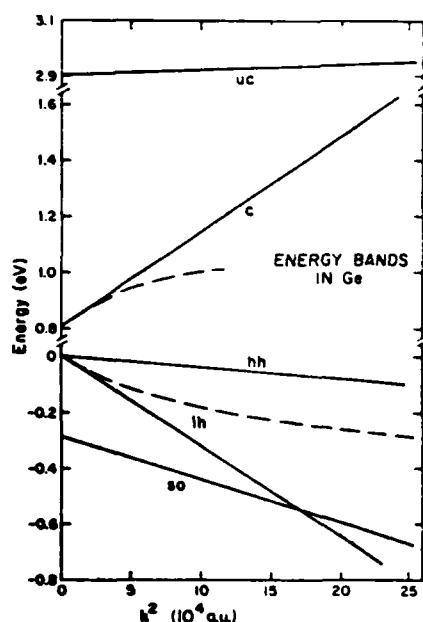


FIG. 1. Band structure of Ge including light-hole (lh), heavy-hole (hh), split-off (so), conduction (c), and upper conduction (uc) bands. The solid curves give the effective-mass approximation. The dashed curves are more realistic approximations for the lh and c bands.

one step is allowed (does not vanish for states at the center of the band) and the other is forbidden (vanishes at the center of the band). There are no allowed-allowed transitions in Ge. By including

the bands mentioned, we consider all possible transitions involving intermediate states within 10 eV of the valence edge. We use the spherical model of Baldereschi and Lipari¹¹ to describe the valence states. This allows us to include their degeneracy properly but not their anisotropy. For comparison we also perform the calculations assuming that the heavy- and light-hole bands are degenerate and can be described by a single effective mass. This permits us to determine the contribution of the valence-band structure to the results. Finally we study the effect of going beyond the effective-mass approximation for the energy bands. This was done recently for the zinc-blende semiconductors,⁶ and large increases in K_2 resulted when nonparabolic bands were used.

In Sec. III we present the results. When all of the contributions are included properly we obtain results which are 25% lower than Gibson's results. In view of the uncertainties in the experimental results and in some of the parameters used, this agreement is quite satisfactory. Exciton effects ignored in the simple-band model do not appear to make as large a contribution as suggested by Lee and Fan for the zinc-blende semiconductors. We present final conclusions in Sec. IV.

II. THEORY

For light with a frequency ω and polarization $\hat{\eta}$, the two-photon transition rate is given in second-order perturbation theory by

$$T = \frac{2\pi}{\hbar} \left(\frac{4\pi^2 e^4 I^2}{\epsilon c^2 \omega^2 m^4} \right) \sum_{c,v} \int \frac{d^3 k}{(2\pi)^3} \left| \sum_J \frac{\langle c | \hat{\eta} \cdot \hat{p} | J \rangle \langle J | \hat{\eta} \cdot \hat{p} | v \rangle}{\epsilon_J(\vec{k}) - \epsilon_v(\vec{k}) - \hbar\omega} \right|^2 \delta(2\hbar\omega - \epsilon_c(\vec{k}) - \epsilon_v(\vec{k})). \quad (1)$$

We do not consider exciton effects^{11,12} in this paper so the states in Eq. (1) refer to single-particle band states with energies $\epsilon(\vec{k})$. The sums are over valence and conduction states involved as initial and final states and over intermediate states J . Since we have direct double transitions, \vec{k} denotes the wave vector of the states $|c\rangle$, $|v\rangle$, and $|J\rangle$ involved in the transition. I is the beam intensity, ϵ the dielectric function, and m the free-electron mass. The two-photon absorption coefficient K_2 is given by

$$K_2 = 2\hbar\omega T / I^2. \quad (2)$$

We assume that the beam is randomly polarized. Thus our final results are averaged over all possible polarizations.

We use $\vec{k} \cdot \hat{p}$ perturbation theory to describe the wave functions to first order in \vec{k} . This is necessary because the first-order states of the two-step

transitions are described by the first-order corrections to the wave functions. The basis states for the perturbation theory are those at $\vec{k} = 0$. We use the basis set of Fawcett.¹³ The matrix elements of Eq. (1) and those needed in the $\vec{k} \cdot \hat{p}$ theory are evaluated using the experimentally determined matrix elements $\langle P | = 0, 0, 0 | k_x, k_y, k_z \rangle$ and $q = 0.5622 \hbar^2 / m\Gamma_0$. The red c and so bands remain doubly degenerate for $\vec{k} \neq 0$. We also treat the uc bands as if they remain degenerate since their contribution to K_2 is small. As a result, the changes in the c, so, and uc wave functions for $\vec{k} \neq 0$ can be found using standard first-order perturbation theory. The energies are given in the effective-mass approximation by second-order perturbation theory. To second order the c and so bands remain degenerate as they should but the uc bands split. As mentioned, we ignore this splitting by assuming a single uc effective mass. In Table I

TABLE I. Energy gaps E_g and effective masses m_* of electron states in the conduction (c) and upper conduction (uc) bands and of holes in the heavy-hole (hh), light-hole (lh), and split-off (so) bands. Energies are measured relative to the valence-band maximum and are in eV.

α	so	lh	hh	c	uc
E_g	0.29	0.00	0.00	0.805	2.9
m_*/m	0.09	0.042	0.33	0.04	0.64

we list the effective masses and energy gaps.

The degeneracy of the lh and hh states is also lifted for $k \neq 0$. This cannot be ignored as it was for the uc band since the valence states are the initial states of the absorption process. Consequently, we apply second-order degenerate perturbation theory to find the correct combinations of valence basis states that lift the degeneracy for each $\vec{k} \neq 0$. When this is done the energy bands are no longer spherically symmetric. This makes the evaluation of Eq. (1) extremely complicated. To simplify the calculation we use the spherical model of Baldereschi and Lipari¹⁰ to find the valence states. In this model the degeneracy of the valence bands is accounted for, but the energies are no longer anisotropic.

In the spherical model the effective Hamiltonian of second-order degenerate perturbation theory is written

$$H = -\alpha k^2 - \xi (\vec{k} \cdot \vec{J})^2, \quad \alpha > -\frac{9}{4}\xi > 0 \quad (3)$$

when terms which lead to the anisotropy are ignored. \vec{J} is the spin operator for a spin- $\frac{1}{2}$ system. The valence basis states $|v_i\rangle$, $i = 1$ to 4, that lift the degeneracy when, for example, $\vec{k} = k\hat{z}$ can be written in terms of Fawcett's states. In this representation J_z is diagonal and the states ($i = 1, 4$) for $J_z = \pm\frac{1}{2}$ correspond to the heavy-hole states while the $J_z = \pm\frac{1}{2}$ states are the light-hole states. For $\vec{k} \neq k\hat{z}$, H is diagonalized by a rotation. If θ is the angle between \vec{k} and \hat{z} and ϕ is the azimuthal angle, then H is put in diagonal form $U^\dagger H U$ by the rotation operators $U_\theta = \exp(i\theta J_y)$ and $U_\phi = \exp(i\phi J_z)$ which diagonalize the component of \vec{J} parallel to \vec{k} . The new basis states $|v_j\rangle$ which lift the degeneracy for wave vectors in the direction \vec{k} are given by rotating the basis states for $k = \hat{z}$:

$$|v_j\rangle = \sum_i |v_i\rangle (U_{\theta\phi}^\dagger)_{ji}, \quad (4)$$

where $j = 1, 4$ for the heavy-hole states and is 2 or 3 for the light-hole states. Once the appropriate choice of basis states for a particular direction of \vec{k} has been made, the valence wave functions, including the first-order correction which con-

tributes to the momentum matrix elements, are given by standard $\vec{k} \cdot \vec{p}$ theory

$$|v_i\rangle = |v_i\rangle + \sum_j \frac{\langle v_j | \vec{k} \cdot \vec{p} | v_i \rangle}{E_i - E_j} |v_j\rangle, \quad (5)$$

where the sum is over the c, uc, and so basis states. In this model the energy is again given by the effective-mass approximation. The effective masses are given in Table I.

When we use the effective-mass energies the kinetic energy of the electron-hole pair created by the two-photon absorption is $\epsilon_{eh} = \hbar^2 k^2 / 2\mu_{eh}$, where $1/\mu_{eh} = 1/m_c + 1/m_v$ and m_c and m_v are the effective masses of the conduction band and a particular valence band. We then get the usual $(\epsilon_{eh})^{1/2}$ for the density of electron-hole states. Since the amplitude for the two-step process is proportional to k , the transition rate from a particular valence band will depend on k^4 . The value of k is fixed by energy conservation and gives a transition rate proportional to $(\mu_{eh})^{3/2} (2\hbar\omega - E_g)^{1/2}$. Because $(\mu_{hh})^{3/2}$ is four times larger than $(\mu_{lh})^{3/2}$, the hh band should be much more important in the absorption process. Consequently, it is important that we treat the distinction between the two valence bands accurately.

We also consider the effect of using realistic energy bands. The lower dashed curve of Fig. 1 actually gives a better description of the lh band, as inspection of Fawcett's results¹¹ shows. This band does not intersect the so band as the effective-mass approximation does and the apparent effective mass is larger. Consequently, the use of the more realistic lh energy band should increase the contribution of the lh band to the transition rate. A study of Fawcett's results also shows that the conduction band is nonparabolic. However, the modification he calculated does not appear to be as large for the c band as for the lh band. Calculations will show, however, that the inclusion of the nonparabolicity of the conduction band in the evaluation of transition rates is more crucial than a proper treatment of the lh band.

To obtain a simple analytic expression for a realistic lh band for use in these calculations, we assume that it has the form

$$\epsilon_{lh}(k) = -\frac{\hbar^2 k^2}{2m_{lh}} + \left[(\Delta E)^2 + \left(\frac{\hbar^2 k^2}{2\Delta m_{lh}} \right)^2 \right]^{1/2} - \Delta E, \quad (6)$$

The factor $\Delta E(\Delta m_{lh})^2$ was determined by requiring that Eq. (6) give the same k^4 correction as obtained from fourth-order perturbation theory. The other constraint applied to determine ΔE and Δm_{lh} was that the new band have the same slope at large k as the hh band. Thus $1/m_c = 1/\Delta m_{lh} = 1/m_{hh}$. This constraint is arbitrary but an inspection of the bands calculated by Fawcett shows that it is rea-

sonable. We find that $\Delta E = 0.2337$ eV and $\Delta m_{\text{th}} = 0.0481m$. The results are given as the lower dashed curve of Fig. 1.

We have not attempted to determine an analytic expression for a realistic c band that would be valid over the entire range of k in Fig. 1. Detailed comparisons of calculated K_2 with Gibson's results are only possible for $\hbar\omega$ within 0.07 eV of the threshold. Moreover, it is not clear what the appropriate simple form should be. However, in the energy range near threshold the following expression is valid:

$$\epsilon_c(k) = \frac{\hbar^2 k^2}{2m} \left(\frac{m}{m_c} + \Delta m_c (ka_0)^2 \right). \quad (7)$$

We use the effective mass of Table I for m_c and Fawcett's value $\Delta m_c = -1.1 \times 10^{-4}$ as an estimate for the coefficient of the k^4 term. At large k Eq. (7) is no longer valid because it overestimates the increase in the effective mass and ϵ_c decreases for increasing k . Even for $(ka_0)^2$ greater than 5×10^4 , the bending of the band shown in Fig. 1 is probably too extreme. However, the comparisons we make with the experimental values will test electron states for $(ka_0)^2$ only up to 4.5×10^4 . In this range we expect Eq. (7) to be an adequate estimate for the mass enhancement.

A comment should be made about the parameters used. The room-temperature energy gaps¹⁴ are used because the data of Gibson were taken at room temperature. An average energy is used for the uc band gap because we ignore the splitting of the uc band. The effective masses do not appear to be temperature dependent. For example, the effective mass of the conduction band is $0.04m$ at both 1.5 K (Ref. 15) and 300 K.¹⁶ Averages of existing experimental masses^{14,17,18} are used for m_{so} , m_{th} , m_{hh} , and m_{uc} . Unfortunately, the value of P that we use is not consistent with $m_c = 0.04m$ if we assume that the second-order perturbation result for ϵ_c gives the correct effective mass

$$\frac{m}{m_c} = 1 + \frac{2P^2 \hbar^2}{3\epsilon_c^2} \left(\frac{2}{E_c} + \frac{1}{E_c + \Delta} \right). \quad (8)$$

This expression gives $m_c = 0.034m$ if $P = 0.6909$ \hbar^2/ma_0 and the room-temperature energy gaps are used. A value of $P = 0.624$ \hbar^2/ma_0 must be used to give $m_c = 0.04m$ using Eq. (8). This value of P is significantly lower than those found experimentally.^{15,17} We perform calculations with this new value for P and for $m_c = 0.034m$ to test the importance of the uncertainties in these parameters.

Actually evaluating the sums in Eq. (1) is extremely cumbersome because a large number of terms are included when the wave functions are found to first order in $\vec{k} \cdot \vec{p}$ theory. Although the sum over conduction states in Eq. (1) is easily

done because the spin-up and spin-down states make the same contribution, the sum over valence states and the intermediate-state sum are difficult to perform. To proceed, we perform the intermediate state sum for fixed c and v . When we integrate over all directions of \vec{k} and average over $\vec{\eta}$, only certain terms of the intermediate-state sum make contributions. These terms are evaluated numerically and their contribution to the transition rate determined. The sum over v is also done numerically. No analytic expression is given for T because it would be very lengthy and not enlightening. Instead, the final results are given in Figs. 2 and 3. There are several techniques which make the evaluation of the sums easier. These are discussed briefly in the Appendix.

III. RESULTS

All of the results presented in Figs. 2 and 3 were found by including the contributions of all bands mentioned as intermediate states and by making the proper distinction between lh and hh states. The solid curve of Fig. 2 was found by using the effective-mass approximation for the bands and by ignoring the k dependence of the energy denominators in Eq. (1). Similar calculations were performed to test the importance of uc and so bands as intermediate states. When the first was ignored K_2 decreased by ten to twenty percent

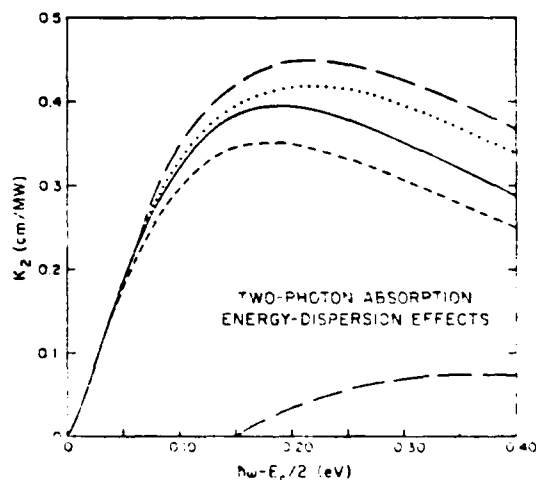


FIG. 2. Energy-dispersion effects on two-photon absorption. The solid curve is calculated by including all bands but by ignoring the k dependence of the energy denominators and by using the effective-mass approximation. The short dashed curve includes the k dependence of the denominators, the long dashed curve uses the realistic lh band, the dotted curve includes both effects. The lower dashed curve is the absorption from the so band including both effects.

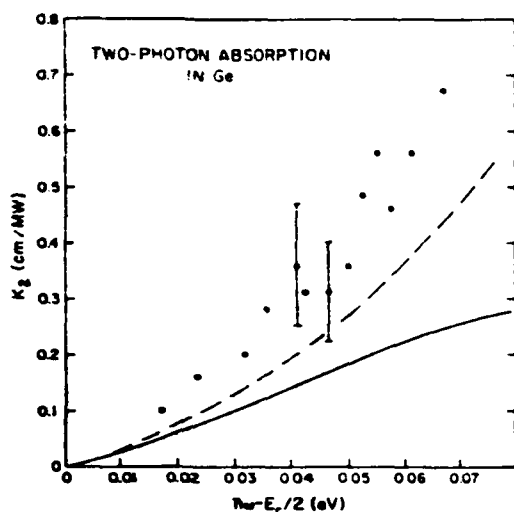


FIG. 3. Comparison of the experimental results of Gibson (Ref. 3) with the simple band-model predictions. The solid curve is found considering all effects except the use of the realistic c band. The dashed curve is found using the realistic c band. The error bars are taken from Gibson's work.

over the energy range shown in Fig. 2. However, when both bands were ignored, K_2 dropped by a factor of 2. Ignoring the so band is equivalent to assuming that $\Delta \gg E_c, \hbar\omega$. Since $\Delta \sim \frac{1}{2}E_c$, this approximation should not be valid in Ge. Although ignoring the so band is a good approximation for some zinc-blende semiconductors² it is a very poor approximation for Ge.

Another calculation was made to determine the importance of including the distinction between lh and hh states. When they are assumed to remain degenerate, the calculation of K_2 is straightforward because the same valence basis states can be used for all directions of \vec{k} . There is then no need to use the spherical model to find new basis states for each direction of \vec{k} . When the lh and hh bands are treated as degenerate we can replace the μ factor in the transition rate by either $\mu_{hh} = \mu_{lh}$ or $[\frac{1}{2}(\mu_{hh} + \mu_{lh})]^{1/2}$. In the first case the results are 6% less than the solid curve and in the second case, 15% less. Thus, if we make a fortuitous choice for an average μ (i.e., we do not replace it with $\mu_{hh}^{1/2}$ or $\mu_{lh}^{1/2}$), then ignoring the distinction between lh and hh bands does not crucially affect K_2 .

In Fig. 2 we show the effect of including the k dependence in the energy denominators (in the manner discussed in the Appendix) and of using the realistic energy band for the light holes. As expected, these contributions are only important away from the threshold. In the energy range considered, the corrections are only fifteen percent. In-

cluding the k dependence of the denominators lowers the results. Using a more realistic lh band increases the contribution of the lh band because the lh density of states and the k in the matrix element increase. The effects of including the k dependence of the denominators and using the realistic lh band compete against each other. A calculation which includes both differs little from one which includes neither in the energy range up to 0.2 eV above threshold. Also shown in Fig. 2 is the absorption coefficient for transitions starting from the so band. The shape is similar to that of the other absorption coefficients. The transition rate is lower because the density of so states is lower than that of hh states. The increase in energy gap also decreases the transition rate.

Different values of P and m_c were used to test their effect on K_2 . Specifically, one calculation was made with m_c reduced to $0.034m$ and another with $P = 0.624 \hbar^2/m$. In these calculations the k dependence of the energy denominators was included and the realistic lh band was used. The new values of P and m_c are too low to be reliable; but, as mentioned, they are needed if Eq. (8) is to give an m_c consistent with the P used. Since the absorption coefficient scales very roughly as P^2 and as $m_c^{3/2}$, K_2 decreases when the new parameters are used. In fact, it decreases by 35% for the new value of P and by 20% for the new value of m_c . However, the uncertainty in K_2 should not be as large as this suggests since the actual uncertainty in P and m_c should be much less.

A comparison between the experimental results of Gibson³ and the calculation that includes the realistic lh band, the k dependence of the denominators, standard parameters, and the distinction between lh and hh bands is shown in Fig. 3. Our comparison is limited because no data are available for $\hbar\omega$ more than 0.07 eV from the threshold. Obviously, even when the uncertainty in the data is considered, the predictions are too low by a factor of about 2. The agreement is adequate near threshold but gets worse 0.05 eV beyond the threshold. The more rapid rise beyond 0.05 eV is not predicted by the calculation using the simple c band. However, when the nonparabolic conduction band is used, a large enhancement of the calculated absorption occurs. In view of the uncertainty in the experimental results, the parameters used and the approximations made, the agreement between this calculation and the experimental results is quite satisfactory. Most importantly, the more rapid rise in K_2 at higher energies is evident. This occurs because the apparent effective mass of the c band increases for increasing $\hbar\omega$. This effect of the nonparabolicity of the c band is especially important for two-photon transitions in which

scales roughly as the $\frac{1}{2}$ power of the apparent effective conduction mass rather than as the $\frac{1}{4}$ power as in single-photon absorption. Consequently, the two-photon absorption should more readily reveal the contribution of the nonparabolicity. This is apparent from Fig. 3. Because we do not determine a realistic c band valid for large k , we do not determine the shape or magnitude of the absorption coefficient at large energies.

Zubov¹ measured K_2 at 2.36 μm to be 1.0 cm^2/MW . At this energy (0.518 eV) we predict K_2 to be only 0.4 cm^2/MW when we use the effective-mass approximation. However, Zubov obtained the experimental value without correcting for the generated carrier absorption. As Gibson has shown, this leads to K_2 values which are too large. Moreover, use of the nonparabolic c band can increase the calculated absorption coefficient by more than a factor of 2 for $\hbar\omega$ greater than 0.05 eV from threshold. Thus the simple band model should be consistent with Zubov's result provided that realistic bands are used.

We should note that no attempt has been made to include higher-order corrections to the matrix elements, even though it is apparent that higher-order corrections to the effective masses are significant. Unfortunately too many terms would have to be evaluated to make inclusion of these higher-order corrections feasible.

IV. CONCLUSIONS

We have presented a simple band-model calculation of the two-photon absorption in Ge. The calculation treats the degeneracy of the valence bands correctly and includes all allowed transitions involving states within 10 eV of the valence edge. In addition, the k dependence of the energy denominators is treated approximately but adequately and realistic energy bands for c and lh states are used. When all of these contributions are included, the agreement between our results and Gibson's results is good. The two effects which must be included to obtain reliable results are the use of the realistic c energy band and the use of the so band as an intermediate state. The other approximations, ignoring the k dependence of the denominators, ignoring the distinction between lh and hh bands and ignoring the uc band, are all more reasonable.

Several effects have not been considered in the simple band model. No attempt has been made to include exciton effects as done by Lee and Fan. The good agreement that we get with Gibson's results suggests that this effect should be small. Lee and Fan find a large enhancement for some zinc-blende semiconductors when exciton effects

are considered. For example, the exciton effects increase the absorption in ZnTe by a factor of 10 and in GaAs by a factor of 2. In these materials the lowest exciton has a binding energy of 10 and 4.4 meV, respectively, while in Ge it has an energy of only 1.6 meV.¹⁹ For this reason we would further expect exciton effects to be less important in Ge.

The effect on the band states of the intense fields needed to measure two-photon absorption has been ignored. Keldysh²⁰ originally studied the effect of an intense field on electronic transitions. When this theory was applied to two-photon transitions,²¹ the results were typically a factor of 10 lower than measured values and were lower than those calculated with the band model of Basov. Thus it would appear that inclusion of the Keldysh effect would lower our results and worsen the agreement. Although the simple band model appears to be adequate for Ge, the importance of exciton and high-field effects cannot be ruled out. These effects require further consideration.

ACKNOWLEDGMENT

This work has been performed under the auspices of the Air Force Office of Scientific Research through AFOSR Contract No. F49620-78-C-0095.

APPENDIX

We must consider the following operator

$$M_v = \sum_j \frac{\vec{\eta} \cdot \vec{p} \langle j | \mathcal{H} | j \rangle \vec{\eta} \cdot \vec{p}}{\epsilon_j(k) - \epsilon_v(k) - \hbar\omega}. \quad (\text{A1})$$

To determine T , we calculate

$$\sum_v \langle c | M_v | v \rangle \langle v | M_v | c \rangle. \quad (\text{A2})$$

We evaluate M for two simplified cases. In the first case we ignore the k dependence of the energy denominators, using only the energy gaps to evaluate $\epsilon_j(k) - \epsilon_v(k)$. In this case M is the same for lh and hh states. Moreover, in the intermediate-state sum, the sum over lh and hh can be done by ignoring the distinction between lh and hh states when the denominator is the same for both. The same valence basis states can then be used for each wave vector.

We also evaluate M with the k dependence of the denominator included. In this case M_{lh} and M_{hh} are different. However, in the sum over j the sum over lh and hh can only be done simply if the difference in the two bands is still ignored. Thus we make the following approximation:

$$\sum_{j \in \text{lh, hh}} \frac{\tilde{\eta} \cdot \tilde{p} \cdot \mathcal{J} \langle j | \tilde{\eta} \cdot \tilde{p} \rangle}{\epsilon_j(k) - \epsilon_v(k) - \hbar\omega} \\ \approx \frac{1}{2} \left(\sum_{j \in \text{lh, hh}} \tilde{\eta} \cdot \tilde{p} \cdot \mathcal{J} \langle j | \tilde{\eta} \cdot \tilde{p} \rangle \right) \\ \times \left(\frac{1}{\epsilon_{\text{lh}}(k) - \epsilon_v(k) - \hbar\omega} + \frac{1}{\epsilon_{\text{hh}}(k) - \epsilon_v(k) - \hbar\omega} \right). \quad (\text{A3})$$

The results for K_j found using Eq. (A3) do not differ greatly from those found when the k dependence is ignored altogether. Thus we expect Eq. (A3) to give an adequate approximation for the k dependence.

There are several ways to make the evaluation of Eq. (A2) easier. First note that

$$\sum_{j \in \text{hh}} |\langle c | M_{\text{hh}} | v \rangle|^2 = \sum_{v \in \text{lh, hh}} |\langle c | M_{\text{hh}} | v \rangle|^2 - \sum_{v \in \text{lh}} |\langle c | M_{\text{hh}} | v \rangle|^2. \quad (\text{A4})$$

As argued before, when we sum over all lh and hh states and the operator is the same for both, we can ignore the difference in lh and hh states and use the simpler valence basis states. Thus the first term in Eq. (A4) is easier to evaluate. In the second sum we must use the lh states found using the basis states given by Eqs. (4) and (5). However, this sum is easier to perform than the original one over hh states. To see this we need to consider the following.

The matrix operators U_ϕ and U_θ take the following form²²:

$$U_\phi = \begin{pmatrix} e^{i3\phi/2} & 0 & 0 & 0 \\ 0 & e^{i\phi/2} & 0 & 0 \\ 0 & 0 & e^{-i\phi/2} & 0 \\ 0 & 0 & 0 & e^{-i3\phi/2} \end{pmatrix}, \quad (\text{A5})$$

$$U_\theta = \begin{pmatrix} c^3 & \sqrt{3}cs^2 & \sqrt{3}cs^2 & s^3 \\ -\sqrt{3}c^2s & c(1-3s^2) & -s(1-3c^2) & \sqrt{3}cs^2 \\ \sqrt{3}cs^2 & s(1-3c^2) & c(1-3s^2) & \sqrt{3}c^2s \\ -s^3 & \sqrt{3}cs^2 & -\sqrt{3}c^2s & c^3 \end{pmatrix},$$

with $c = \cos(\theta/2)$ and $s = \sin(\theta/2)$. The basis set is

$$|v_1\rangle = \begin{pmatrix} 1 \\ 0 \\ 0 \\ 0 \end{pmatrix}, |v_2\rangle = \begin{pmatrix} 0 \\ 1 \\ 0 \\ 0 \end{pmatrix}, |v_3\rangle = \begin{pmatrix} 0 \\ 0 \\ 1 \\ 0 \end{pmatrix}, |v_4\rangle = \begin{pmatrix} 0 \\ 0 \\ 0 \\ 1 \end{pmatrix}, \quad (\text{A6})$$

where hh basis states for $\vec{k} = k\hat{z}$ are $|v_1\rangle$ and $|v_4\rangle$ while $|v_2\rangle$ and $|v_3\rangle$ are the corresponding lh states. At other \vec{k} , the lh basis states are given by Eq. (4) with $j = 2, 3$.

The wave function is given to first order in k by Eq. (5). This can be written as

$$|v, \vec{k}\rangle = B(\vec{k}) |v, \hat{k}\rangle, \quad (\text{A7})$$

with

$$B(\vec{k}) = 1 + \sum_B \frac{1}{2} \frac{(\beta \hbar \vec{k} \cdot \tilde{p})/m}{-\epsilon_B}.$$

The sum over lh can now be written as

$$\sum_{j=2,3} |v, \vec{k}\rangle \langle v, \vec{k}| = B(\vec{k}) \left(\sum_{j=2,3} |v, \hat{k}\rangle \langle v, \hat{k}| \right) B^*(\vec{k}). \quad (\text{A8})$$

But

$$\sum_{j=2,3} |v, \hat{k}\rangle \langle v, \hat{k}| \\ = \sum_{j=2,3; i, k=1,2,3,4} |v_i\rangle (U_{-\phi} U_{-\theta})_{ij} (U_\theta U_\phi)_{jk} \langle v_k|. \quad (\text{A9})$$

The product of the rotation operators can be simplified in the following way:

$$U_{-\phi} U_{-\theta} \begin{pmatrix} 0 & 0 & 0 & 0 \\ 0 & 1 & 0 & 0 \\ 0 & 0 & 1 & 0 \\ 0 & 0 & 0 & 0 \end{pmatrix} U_\theta U_\phi = \frac{1}{k^2} \begin{pmatrix} \frac{1}{2} k_- k_+ & -(\frac{1}{2})^{1/2} k_- k_z & \frac{-\sqrt{3}}{2} k_-^2 & 0 \\ -(\frac{1}{2})^{1/2} k_- k_z & k_z^2 + \frac{1}{2} k_- k_+ & 0 & \frac{-\sqrt{3}}{2} k_-^2 \\ \frac{-\sqrt{3}}{2} k_-^2 & 0 & k_z^2 + \frac{1}{2} k_- k_+ & (\frac{1}{2})^{1/2} k_- k_z \\ 0 & \frac{-\sqrt{3}}{2} k_-^2 & (\frac{1}{2})^{1/2} k_- k_z & \frac{1}{2} k_- k_+ \end{pmatrix} = A A^\dagger, \quad (\text{A10})$$

where

$$A = \frac{1}{k} \begin{bmatrix} 0 & (\frac{1}{2})^{1/2} k_- & 0 & 0 \\ 0 & -k_+ & -k_-/\sqrt{2} & 0 \\ 0 & -k_+/\sqrt{2} & k_+ & 0 \\ 0 & 0 & (\frac{1}{2})^{1/2} k_+ & 0 \end{bmatrix} \quad (A11)$$

and $k_{\pm} = (k_x \pm i k_y)/\sqrt{2}$.

The operator A defines new basis states for the lh band

$$|v, \hat{k}\rangle = \sum_i |v_i\rangle A_{i,j} \quad \text{for } j = 2, 3. \quad (A12)$$

These states give the same sum over lh states and yet are simpler to work with. A has a simpler form than U_{-} or U_{+} and some of the elements in A vanish. Moreover, the elements of A are written in terms of k_+ and k_- . When Eq. (A2) is integrated over all directions of \vec{k} only terms with even powers of k_+ and matching powers of k_- and k_+ will contribute. The use of Eq. (A11) makes it easier to identify those terms in Eq. (A2) that must be evaluated.

- ¹B. V. Zubov, L. A. Kulevskii, V. P. Makarov, T. M. Murina, and A. M. Prokhorov, *Zh. Eksp. Teor. Fiz. Pis'ma Red.* **9**, 221 (1969) [*JETP Lett.* **9**, 130 (1969)].
- ²R. G. Wenzel, G. P. Arnold, and N. R. Greiner, *Appl. Opt.* **12**, 2245 (1973).
- ³A. F. Gibson, C. B. Hatch, P. N. D. Maggs, D. R. Tilley, and A. C. Walker, *J. Phys. C* **9**, 3259 (1976).
- ⁴J. M. Doviak, A. F. Gibson, M. F. Kimmitt, and A. C. Walker, *J. Phys. C* **6**, 593 (1973).
- ⁵C. C. Lee and H. Y. Fan, *Phys. Rev. B* **9**, 3502 (1974).
- ⁶C. R. Pidgeon, B. S. Wherrett, A. M. Johnston, J. Dempsey, and A. Miller, *Phys. Rev. Lett.* **42**, 1785 (1979).
- ⁷R. Braumstein and N. Ockman, *Phys. Rev.* **134**, 499 (1964).
- ⁸N. G. Basov, A. Z. Grasyuk, I. G. Zubarev, V. A. Katulin, and O. N. Krokhin, *Zh. Eksp. Teor. Fiz.* **50**, 551 (1966) [*Sov. Phys.—JETP* **23**, 366 (1966)].
- ⁹S. B. Arifzhanov and E. L. Ivchenko, *Fiz. Tverd. Tela (Leningrad)* **17**, 81 (1975) [*Sov. Phys.—Solid State* **17**, 46 (1975)].
- ¹⁰A. Baldereschi and N. O. Lipari, *Phys. Rev. B* **8**, 2697 (1973).
- ¹¹G. D. Mahan, *Phys. Rev.* **170**, 825 (1968).
- ¹²R. Loudon, *Proc. R. Soc. London* **90**, 952 (1962).
- ¹³W. Fawcett, *Proc. Phys. Soc.* **85**, 931 (1965).
- ¹⁴M. Neuberger, *Handbook of Electronic Materials* (Plenum, New York, 1971), Vol. 5.
- ¹⁵M. Rouzeyre, H. Mathieu, D. Auvergne, and J. Camassel, *Solid State Commun.* **7**, 1219 (1969).
- ¹⁶S. H. Groves, C. R. Pidgeon, and J. Feinleib, *Phys. Rev. Lett.* **17**, 643 (1966).
- ¹⁷P. Lawaetz, *Phys. Rev. B* **4**, 3460 (1971).
- ¹⁸G. Dresselhaus and M. S. Dresselhaus, *Phys. Rev.* **160**, 649 (1967).
- ¹⁹A. Baldereschi and N. O. Lipari, *Phys. Rev. B* **3**, 439 (1971).
- ²⁰L. V. Keldysh, *Zh. Eksp. Teor. Fiz.* **47**, 1945 (1964) [*Sov. Phys.—JETP* **20**, 1307 (1965)].
- ²¹S. S. Mitra, L. M. Narducci, R. A. Shatas, Y. E. Tsay, and A. Vaidyanathan, *Appl. Opt.* **14**, 3038 (1975).
- ²²A. R. Edmonds, *Angular Momentum in Quantum Mechanics* (Princeton University, Princeton, N. J., 1957).

VI. INTERACTIONS OF INTENSE 2.7 μ m PICOSECOND

LASER PULSES WITH GERMANIUM

G. W. Bryant⁺⁺, A. Schmid⁺, and P. Braunlich⁺

Physics Department

Washington State University

and

P. Kelly and D. Ritchie

Physics Department

National Research Council of Canada

* Present address: Surface Science Division, National Bureau of Standards, Washington, D. C. 20234

+ Supported by AFOSR Contract F 49620-78-C-0095
Paper presented at the "Twelfth Annual Symposium on Optical Materials for High Power Lasers", Sept. 30 - Oct. 1, 1980 Boulder, Colorado

I. Introduction

Laser damage and laser annealing in semiconductors have recently lent a great deal of motivation to fundamental studies of the interaction of laser pulses with semiconductors such as Ge, Si, GaAs, etc. . In addition to the understanding of free carrier kinetics and the interplay between heated carriers and the lattice background an analysis of the dynamic laser self-action has now become mandatory if a comprehensive insight into the intricate laser pulse - semiconductor processes is to be gained.

Laser self-action can best be described by recalling that the dielectric function , and in turn the refractive index, for each material is strongly dependent on the carrier distribution. Thus a change in this distribution due to the presence of an external photon field, due to changes in temperature or due to other influences will effectively change the geometrical optical properties of the material. Frequency shifts, self-focusing, self-defocusing and changes in shape of laser pulses and possibly the whole phenomenon of laser damage in semiconductors may all lend themselves to explanations in terms of such dynamic refractive index changes. We present here a status report on an effort aimed at simulating such spatio-temporal changes in Ge which is exposed to 2.7 μm picosecond laser pulses. We will limit our discussion to temporal aspects only and will describe the entire spatial dynamics elsewhere. However, we will be able to address and answer an important question which has recently been raised. That is, Ge has been claimed to possess unusually high damage thresholds at 2.7 μm and 10.6 μm . We will comment on the possible cause for this effect.

II. Damage Criterium

From the outset we assume an idealized crystal. We disregard therefore any possible contribution to damage by inclusions or by other defects. We concentrate instead on heating of the phonon system which comprises an Einstein-type optical phonon system and a Debye-type acoustical phonon system. The two systems are coupled to each other and independently linked to the carrier systems, i.e. the photoexcited free carriers and holes. Each phonon system contributes to the temperature dependent mean square displacements of lattice constituents, $\langle u^2 \rangle_{op}(T)$ and $\langle u^2 \rangle_{ac}(T)$ respectively. If these two mean square displacements taken together become excessive (i.e. larger than the displacement sum at equilibrium melting temperature T_m)

$$\langle u^2 \rangle_{ac}(T_{ac}) + \langle u^2 \rangle_{op}(T_{op}) > \langle u^2 \rangle_{ac}(T_m) + \langle u^2 \rangle_{op}(T_m)$$

permanent lattice modifications are expected and damage is assumed to occur. Our purpose is, therefore, to perform calculations which permit monitoring of the temperatures in the two phonon systems during the passage of a laser pulse. Note that, according to our criterium the required damage temperature has to exceed 5600°K in the optical phonon system alone if for some reason the acoustical phonon system should prove unable to significantly warm up during the pulse length of a picosecond pulse. Note also that the damaging temperature T_{op} calculated under these circumstances is still an approximation which will require further refinement. For example, we presently evaluate mean square displacements without accounting for anharmonic effects.

In order to calculate the phonon system temperatures and their change during the history of a laser pulse detailed information about electron-electron, electron-phonon and hole-phonon interactions in the system is required.

In the next section we will briefly review in form of a block diagram how the energy absorbed from the laser field ultimately ends up in the optical and acoustical phonon systems. We will thereby specify some details of the different interactions.

III. Energy Transport

Photo-excitation in Ge at 2.7μ leads to the formation of electron-hole pairs via direct two photon interband absorption. The transition rates for this process were evaluated in the recent work by Bryant⁽¹⁾. The dynamics of photoexcited electrons and holes in Ge has been studied in considerable detail by Elci, Scully, Smirl and Matter⁽²⁾. Our present model uses their results modified to take account of the two separate phonon systems⁽³⁾ and disregards Auger recombination for the time being. However, as our results will show, this simplification is no longer justified since appreciable heating at 2.7μ requires very high local free carrier concentrations, a condition under which Auger recombination is most effective. The next phase of program development will therefore include this effect as well. A further refinement, which is already part of the model, accounts without averaging for all the conduction band valleys and allows for single-photon hole transitions between different valence bands when the light and heavy hole bands are highly depleted.

In our block diagram (Fig. 1) the sources of energy gain from the laser field are listed on top. In addition to two-photon absorption we consider free carrier absorption (FCA) and free hole absorption (FHA), which are both single photon absorption processes involving phonons for momentum conservation, and hole transitions to the split-off band. The last process does, of course, not generate any new holes but increases their energy instead.

The respective interband transitions are shown in Fig. 2. Excited carriers in the central conduction band valley are assumed to rapidly scatter into the side valleys (via electron-phonon scattering) where they thermalize into a quasi-Fermi distribution of temperature T_e . Note that scattering into the side valleys removes electrons from states which are the final states of the two-photon absorption process across the band gap and that the build-up of carriers in the side valleys thus regulates availability of those states and therefore the transition rate. Proper accounting of the availability of states demands as realistic a description of the bands as possible. Similarly, the light and heavy hole valence bands have to be treated as non-degenerate if hole transitions into the split-off band are to be treated correctly.

Phonon emission and absorption leads to carrier cooling by intravalley relaxation. Since the optical phonons have a stronger coupling to the heated carriers⁽³⁾, this relaxation will bring about a slightly faster temperature rise in the optical phonon subsystem than in the acoustical one. Subsequently optical phonons decay into acoustical phonons with a characteristic, temperature independent time constant τ ⁽⁴⁾. The temperature rise in the two systems is monitored in order to detect damage according to Section 2.

The two temperature rises are given by

$$\frac{dT_{op}}{dt} = \frac{2}{c_v} \frac{du_{op}}{dt} - \left(\frac{\partial T_{op}}{\partial N_{op}} \right) \frac{N_{op}(T_{op}) - N_{op}(T_{ac})}{\tau}$$

and

$$\frac{dT_{ac}}{dt} = \frac{2}{c_v} \frac{du_{ac}}{dt} + h\Omega_0 \frac{N_{op}(T_{op}) - N_{op}(T_{ac})}{\tau}$$

where optical and acoustical phonons have each been assigned half the contribution to the total specific heat c_v and where τ is the optical phonon decay lifetime, $N_{op}(T)$ the optical phonon number at temperature T and of uniform energy $\hbar\Omega_o$, and du/dt the respective rate of change in energy density due to energy transfer during free carrier absorption and intravalley relaxation. These energy transfer rates depend on the carrier and hole density and respective energy distributions and therefore on the temperature of the electron and hole system. We will refrain from presenting the pertinent expressions here since they are rather involved and will be published when we have arrived at a comprehensive picture of the laser-semiconductor interaction. It suffices to say that the numerical procedure of modeling the temporal aspects of this interaction involves solving a set of five coupled differential equations each of which contains integrations over the carrier distributions in each valley and each valence band.

IV. Results

We have tested the damaging properties of several 2.7 μ laser pulses in the picosecond regime. Pulse lengths of 5, 10, and 20 psec were chosen at peak fluxes of 10^{28} , 10^{29} and 10^{30} photons per cm^2 and sec, respectively. For reasons of operational simplicity the Gaussian temporal waveform of each pulse was truncated at the $1/e^3$ peak intensity points. Initial conditions for the carrier chemical potential and carrier temperature were determined by long hand and the dependence of the final results on the precise choice of these initial conditions was tested.

We present in Fig. 3 and 4 the free electron density N_e and free carrier energy density ξ per unit volume as both evolve during a 10^{28} photons/ cm^2 sec peak flux, 20 psec pulse. Without an effective drain on the

carriers, such as Auger recombination, one finds, as expected, a rapid increase in the carrier density in the early part of the pulse without any significant reduction in the later part. A minute reduction which is noticeable only numerically and not on the graph of Fig. 3 accounts for two-photon stimulated emission which is included in our two-photon transition probability. The energy density ξ of the free carriers and holes shown in Fig. 4 exhibits similar behaviour in the first half of the pulse. Along the trailing edge of the pulse the energy density diminishes first on account of the two phonon systems and stabilizes seemingly towards the end of the pulse. This effect is a model artefact and can be explained in conjunction with Fig. 5. There the systems' temperatures are plotted for the free carrier and optical phonon systems as a function of time. The free carriers heat in accordance with the instantaneous availability of photons and of final states for transitions. The electron temperature follows therefore a modified Gaussian as one would expect for a temporal Gaussian intensity distribution in the laser pulse. However, since the temperature rise is accompanied by additional free carrier generation while the electron temperature decline is lacking a corresponding recombination process across the band gap, the available conduction band states rapidly fill up during carrier cooling, in the later part of the pulse, thus keeping energy in the electron system which otherwise could be transferred in electron-phonon processes. This also explains why the optical phonon temperature rise proceeds at a less rapid rate in the late part of the pulse than earlier.

We also note that a 10^{23} phot/cm² sec peak flux, 20 psec pulse raises the optical phonon temperature merely to 552 °K. Contrary to some earlier expectations⁽³⁾ however, the acoustical phonon temperature rise does not lag behind the optical one and the two systems' temperatures agree to within

less than 1% over the whole pulse length. The optical phonon temperature does therefore not have to rise to 5600 °K in order for the damaging phase transition to take place.

It is tempting to compare these results with earlier work done at 1.06 μm ⁽²⁾. While we find qualitatively plausible agreement comparison of numbers becomes difficult in light of the different experimental conditions chosen in each model. The work of Reference 2 rests on the assumption of a square pulse, for instance, while the present work assumes a Gaussian temporal profile. Since the dynamic processes are nonlinear no simple scaling relation between the pulse shapes can be established. Our model calculations do, however, confirm that ideal Ge requires very high fluxes even at 2.7 μm for damage to occur. The flux regime of 10^{29} photons/cm² sec at which we predict damage to occur borders on fluxes which in much wider band gap materials, at larger photon energies and under physical processes quite different from the ones considered here also produce damage. These processes have been identified to be highly nonlinear and are thus requiring very high fluxes to come about. In contrast, free carrier generation at 2.7 μm in Ge is only a two-photon process and damage due to these carriers was intuitively expected to ensue at much lower fluxes. Our calculations show that for ideal Ge such expectations are unjustified.

In the next phase of our calculations several additional physical phenomena will be included into the model. Among them are Auger recombination of free carriers and band gap narrowing effects⁽⁵⁾ as well as the dynamic dielectric constant which will allow a comprehensive spatio-temporal modeling of beam propagation.

This work was supported by AFOSR through Contract #F 49620-78-C-0095.

References

1. Bryant, G. W. Phys. Rev. B 22, 1992 (1980).
2. Elci, A., Scully, M. O., Smirl, A. L. and Matter, J. C., Phys. Rev. B 16, 191 (1977).
3. Van Driel, H. M. Phys. Rev. B 19, 5928 (1979).
4. Safran, S. and Lax, B. J. Phys. Chem. Solids 36, 753 (1975).
5. Ferry, D. K. Phys. Rev. B 18, 7033 (1978).

Figure Captions

1. Block diagram illustrating the energy transfer in highly photo-excited Ge from the $2.7 \mu\text{m}$ photon field to the damage event.
2. Band structure in germanium representing the excitation processes.
3. Electron density $N_e \text{ cm}^{-3}$ as a function of time normalized to the pulse length t_0 for a peak flux of $10^{28} \text{ photons/cm}^2 \text{ sec}$.
4. Variation of free carrier and hole energy density ξ with time normalized to pulse length t_0 for a peak flux of $10^{28} \text{ photons/cm}^2 \text{ sec}$.
5. Variation of electron system temperature T_e (left vertical scale) and optical phonon temperature T_{op} (right vertical scale) with time normalized to pulse length t_0 for same pulse as in Fig. 4.

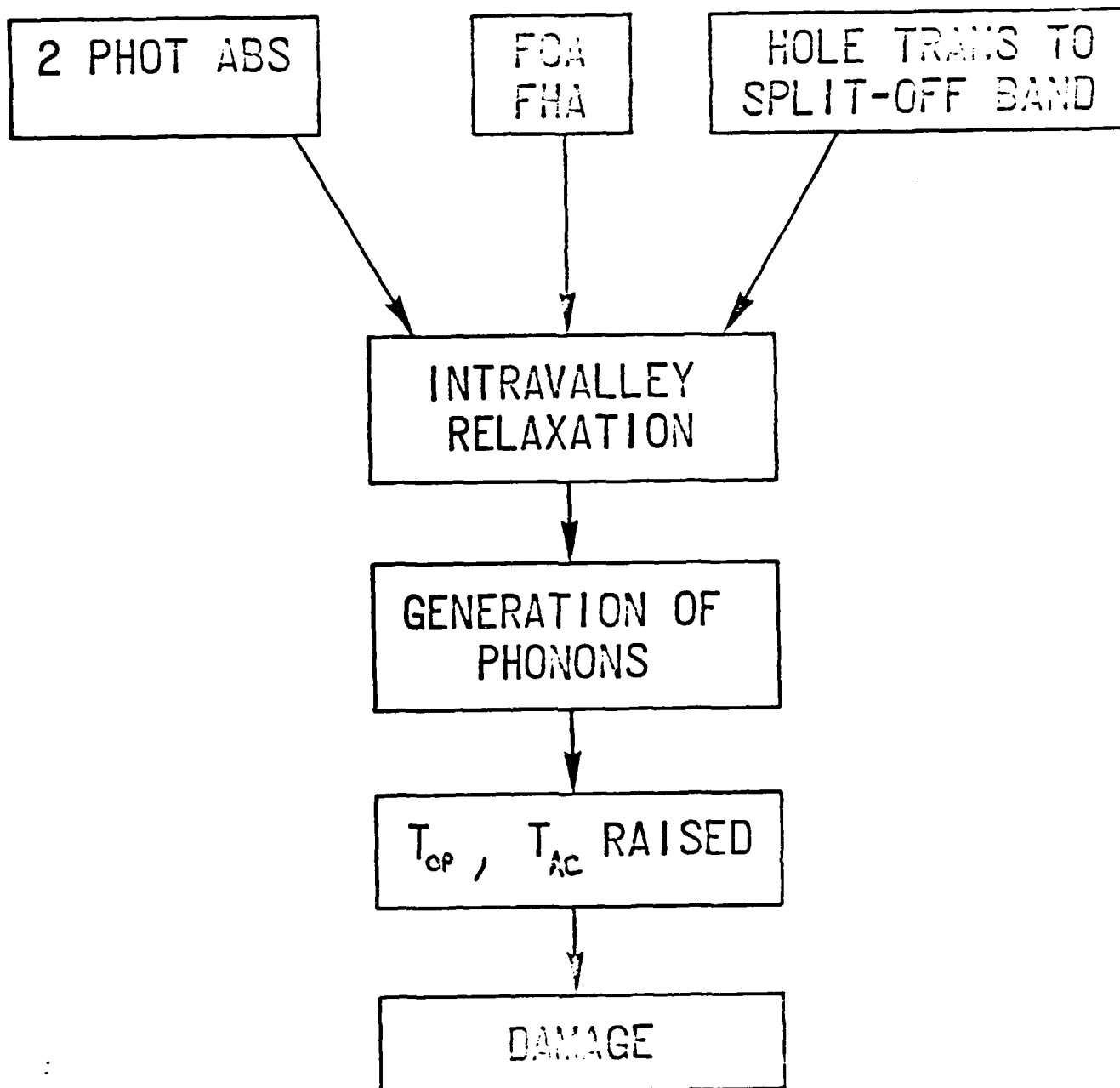


Fig. 1

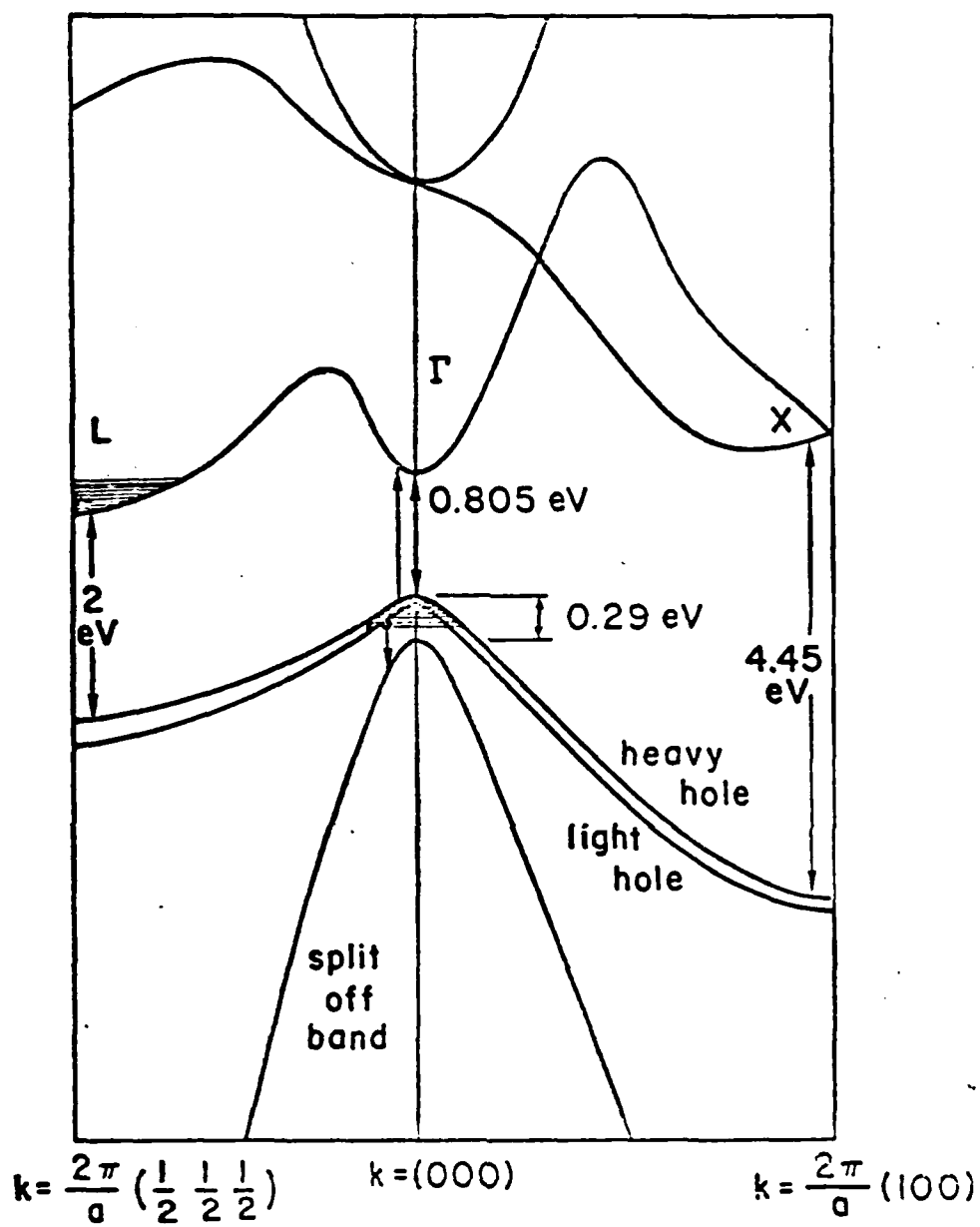


Fig. 2

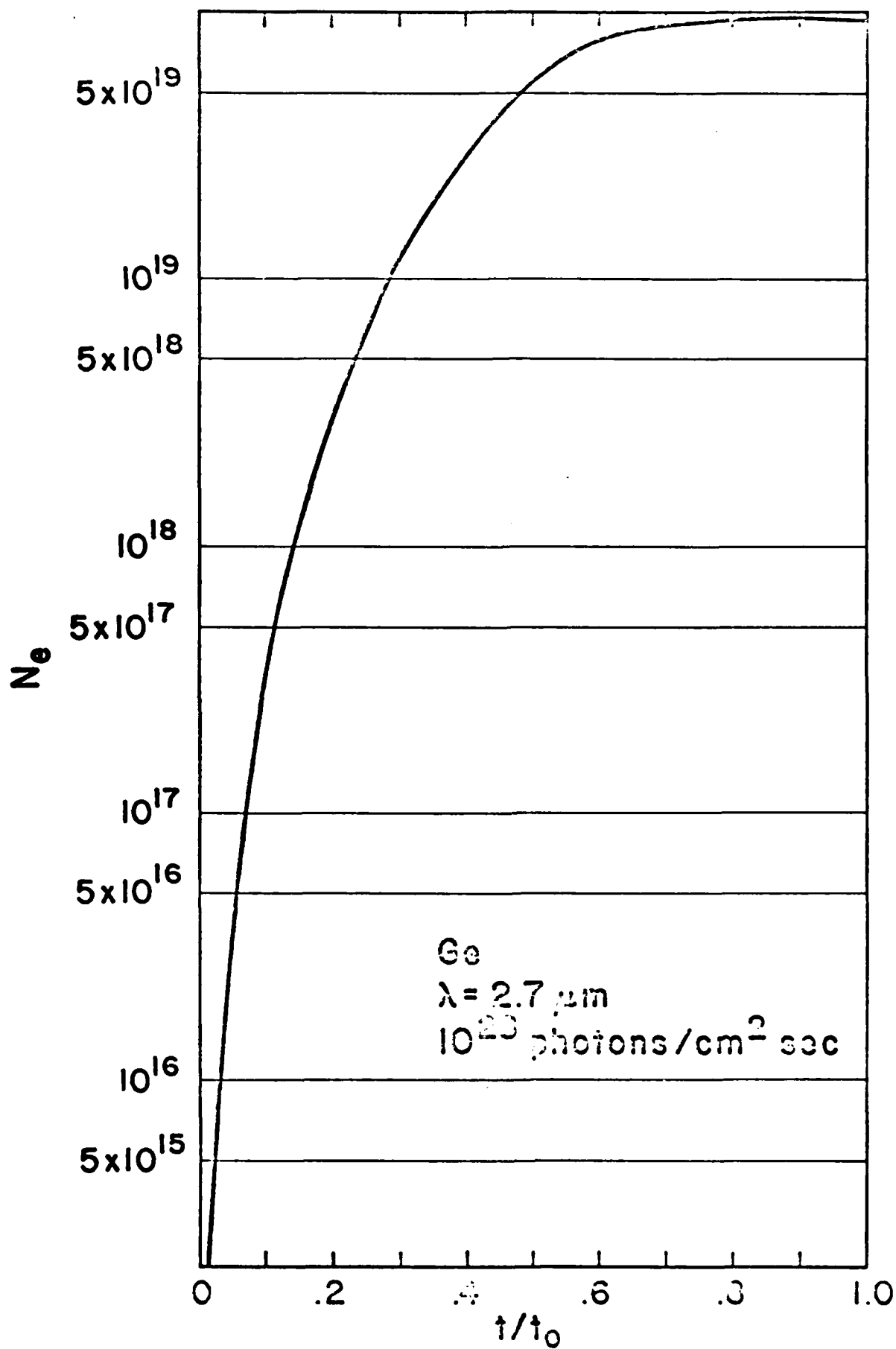


Fig. 3

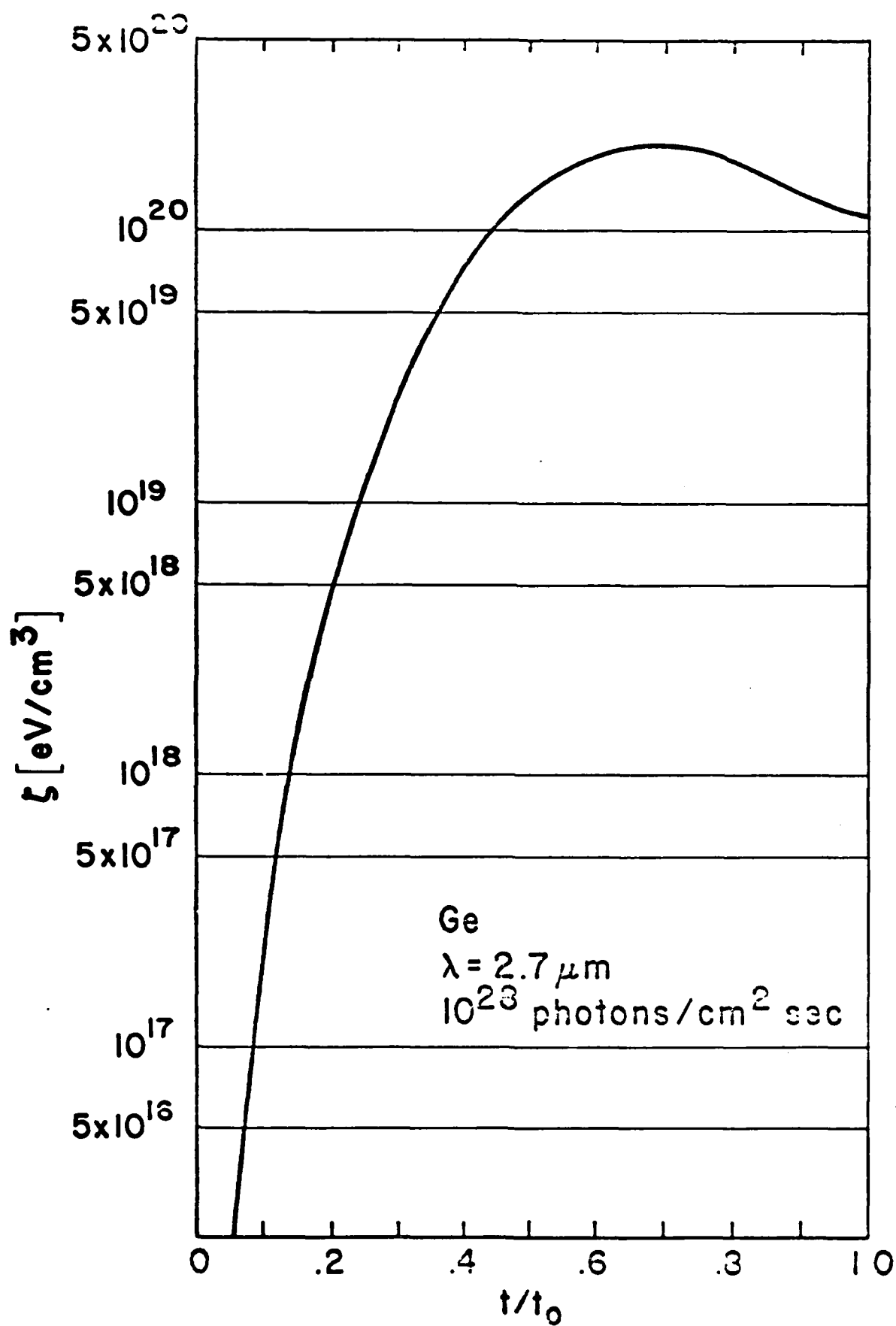


Fig. 4

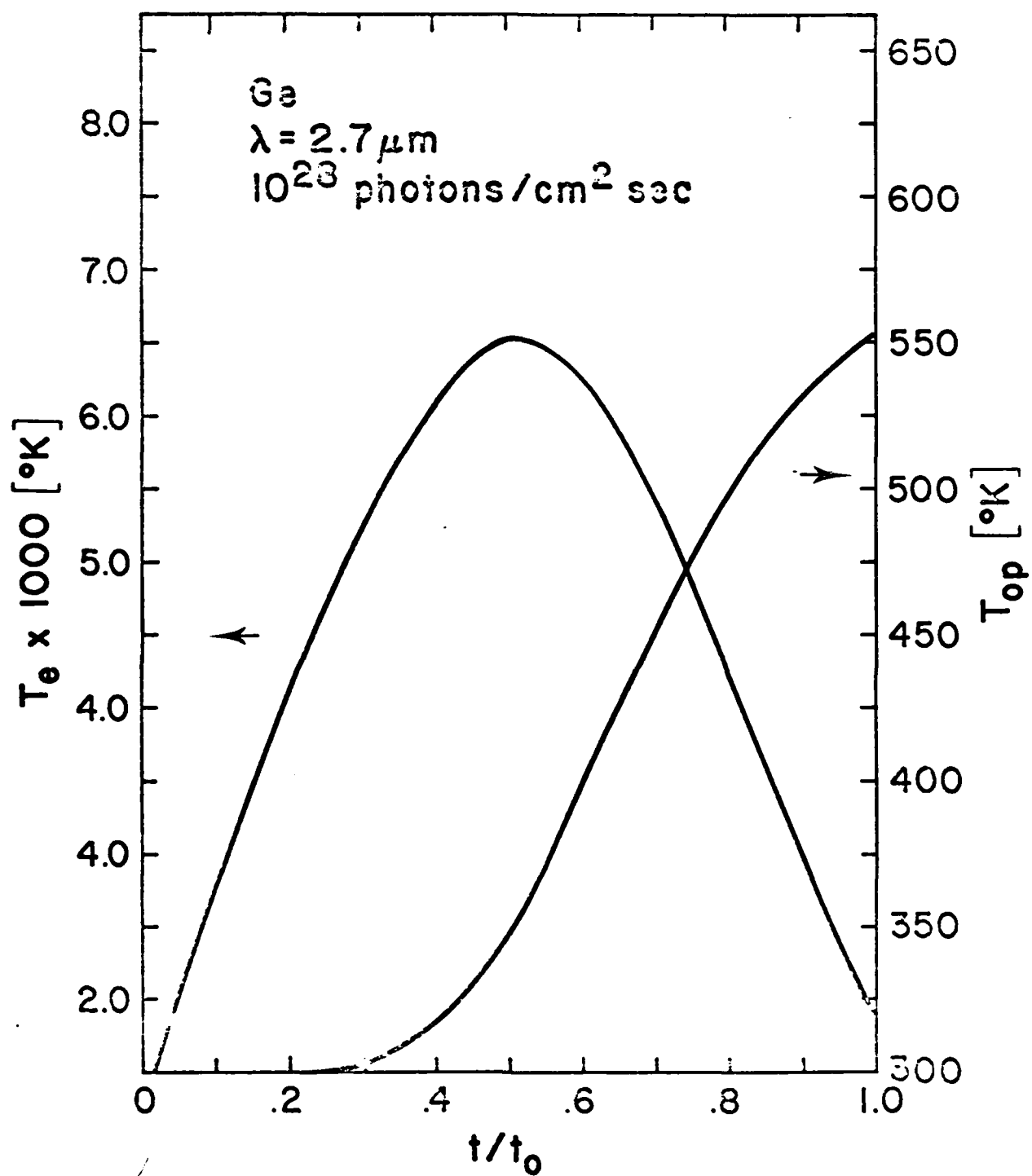


Fig. 5

VII. Planned Publications

1. G. Bryant and others: Presentation at APS Meeting, Phoenix, Arizona, March 1981 (Ge response to 0.45 eV photons).
2. G. Bryant and others: Ge response to 0.45 eV photons, Phys. Rev. B.
3. P. Braunlich and others: Primary defect effects on laser damage computations for NaCl, IEEE (QE) Special Issue on Laser Material Interactions, September 1981.
4. G. Bryant, A. Schmid and others: Formulation of a damage criterium and band gap narrowing in Ge.
5. P. Kelly, G. Bryant and others: Calculation of spatial effects of Ge response to 0.45 eV photons.

VIII. List of Professional Personnel

1. P. Braunlich, Professor of Physics, Principal Investigator
2. A. Schmid, Research Physicist and Assistant Professor, Co-Principal Investigator
3. G. Bryant, Post-Doctoral Research Assistant
4. P. Kelly, NRC (Ottawa, Consultant)
5. D. Ritchie, NRC (Ottawa, Consultant)

IX. Interactions (Coupling Activities)

1. Invited paper on AFOSR sponsored work, Boulder Symposium on High Power Laser Optical Materials (given by P. Kelly, October 1979).
2. Three papers on AFOSR sponsored work presented at Boulder Symposium on High Power Laser Optical Materials (given by P. Braunlich and A. Schmid, October 1980)
3. Participation of Dr. A. Schmid in DOE Workshop on High Power Laser Materials, Aug. 2-6, 1979; presentation on WSU program for the study of the interactions of intense laser light with transparent solids.
4. Participation of Dr. A. Schmid in National Laser Users Facility Workshop, Nov. 29-30, 1979, University of Rochester.
5. Presentation of two papers on AFOSR sponsored work at APS Meeting, N.Y. (given by G. Bryant, March 1979).
6. Seminars on Interactions of Intense Laser Radiation with Transparent Solids at:
 - University of Tübingen, Germany (October 1979)
 - University of Reims, France (January 1980)
 - University of Montpellier, France (February 1980)
 - University of Idaho (April 1980)
 - University of Washington (May 1980)
 - (Presented by P. Braunlich)

Computer Code "PULSE"

PULSE is a two-dimensional photon-particle simulation code based on RAMSES.⁽¹⁾ We have adapted and modified RAMSES to make it suitable for the calculation of the complete spatio-temporal photon-flux distribution as well as that of the photon-induced material modifications which are encountered when a short intense laser pulse propagates through a nominally transparent medium. PULSE is designed to simulate the propagation for any conceivable initial laser intensity profile, beam shape (e.g. focused, parallel or defocused), material distribution (e.g. uniform or layered such as refractive index interfaces, clad optical fibers and coatings on substrates, etc.) and physical mechanism of photon-induced material modifications (e.g. photon-induced changes in the dielectric response function, etc.)

To test the developed code we have so far concentrated on the simulation of an intense frequency-doubled 21 psec pulse from a Nd-glass laser. This pulse is focused through a plane interface into single crystalline NaCl with the aid of a plano-convex lens of 1" focal length. The location of the geometrical focal point is chosen to be 0.2 cm behind the interface inside the crystal (Fig. 1). This configuration is the one used by Smith et al.⁽²⁾ in their studies of the damage threshold in alkali halides at that wavelength.

In the following we will use this particular example to describe the features of PULSE.

In the model of the pulse, energy is carried by a finite number of macroscopic photons whose trajectories through the medium are the object of the calculations to date. A clipped gaussian profile is attributed to the pulse and both the pulse and the medium are considered rotationally symmetric so that energy varies in two dimensions only. A variation in the direction

of propagation corresponds to a time variation and a variation perpendicular to propagation describes the radial properties of the pulse.

In these present calculations the interaction between the photon pulse and the medium involves multiphoton generation of free carriers, n_c , which in turn effects the refractive index n . In addition, a self-focusing term $n_2 E^2$ is added to n , where E is the rms optical field strength. Local variations of n_c , n , and E are calculated as functions of time and the spatial coordinate \vec{r} . The aim of this simulation is to study beam deformation of a focused beam having a clipped Gaussian flux profile.

Initially the photons are distributed uniformly within the pulse length and beam width. They are directed to the focal point and then repositioned to take into account refraction at the plane surface of the interface between vacuum and NaCl ($n_0 = 1.53$). The clipped Gaussian profile is represented as follows: the intensity per cell "k,j" given by

$$I_{k,j} = \frac{cE}{2\pi h_x h_y} \frac{\exp\left\{-\left(\frac{r_{k'}}{R}\right)^2 - \left(\frac{x_j - \alpha x}{x}\right)^2\right\}}{\left[\sum_{k',j'} \frac{r_{k'}}{R} \exp\left\{-\left(\frac{r_{k'}}{R}\right)^2 - \left(\frac{x_{j'} - \alpha x}{x}\right)^2\right\}\right]} \quad 1)$$

Here c is vacuum velocity of light, E the total energy content, h_x , h_y the cell size, R the radial scale factor and $2x$ the pulse length. α is a free parameter used for clipping the Gaussian (1.5 used to date).

For NaCl the local refractive index is obtained from our previous work,⁽³⁾ assuming optical phonon scattering:

$$n(\vec{r}) = n_1(\vec{r}) \left[1 + .5 \sqrt{1 + \frac{\delta \cdot F(\vec{r})}{n_1^2(\vec{r})}} \right]$$

Schematic of Simulated Experimental Arrangement

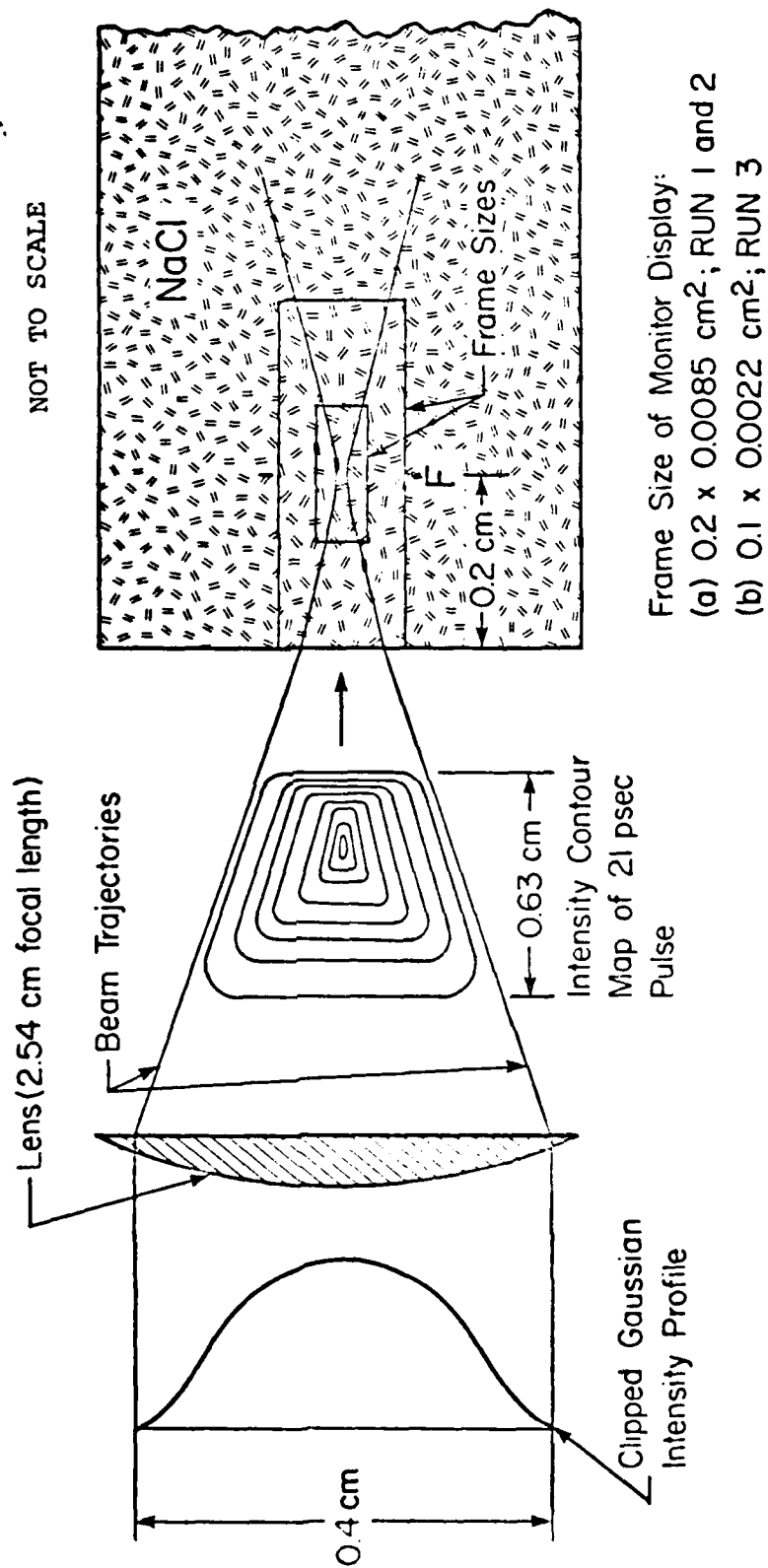


FIG. 1

$F(\vec{r})$ is flux in $\text{cm}^{-2}\text{sec}^{-1}$

$$\delta = 1.737 \times 10^{-33} (\hbar\omega)$$

$$n_1(\vec{r}) = \{0.5 \times [\epsilon_1(\vec{r}) + f(\vec{r})]\}^{1/2}$$

$$f(\vec{r}) = \{\epsilon_1^2(\vec{r}) + \epsilon_2^2(\vec{r})\}^{1/2}$$

$$\epsilon_1(\vec{r}) = n_o^2 - s_w g(\vec{r})$$

$$\epsilon_2(\vec{r}) = \epsilon_{20} s_w g(\vec{r})$$

$$\epsilon_{20} = \delta \cdot (\hbar\omega_L / \hbar\omega)^{3/2}$$

$$\hbar\omega = 2.33 \text{ eV (photon energy),}$$

$$\hbar\omega_L = .03 \text{ eV (phonon energy),}$$

$$N_{vo} = 2.24 \times 10^{22} \text{ cm}^{-3} \text{ (density of valence electrons)}$$

$$s_w = N_{vo} \times 1.839 \times 10^{-21} / (\hbar\omega)^2$$

and $g(\vec{r})$ is the ionization fraction n_c / N_{vo} .

Gradients in $n_c(\vec{r}, t)$ cause gradients in $n(\vec{r}, t)$ which lead to refraction. The photons change directions according to

$$\frac{d\vec{r}}{ds} = \vec{\tau}_1 \cdot (\vec{\tau}_1 \cdot \nabla n)$$

where $\vec{\tau}_1$ are vectors normal to $\vec{\tau}$, the particle directions.

Since the local velocity of light v_g in the medium depends on the refractive index, the group velocity straggling factor β can be computed:

$$\beta(\vec{r}) = v_g(\vec{r})/c$$

$$= n(\vec{r}) + \frac{n_o^2 - \epsilon_1(\vec{r})}{2n_1(\vec{r})} \left[1 + \frac{\left[\epsilon_1(\vec{r}) - \frac{7}{4} \epsilon_{20} \epsilon_2(\vec{r}) \right]}{f(\vec{r})} \right]$$

The multiphoton ionization rate is given by

$$R(\vec{r}) = \sigma_4 (I(\vec{r})/\hbar\omega)^4$$

$$= (S_4 F(\vec{r}))^4$$

($S_4 = 1.951 \times 10^{-28}$ for F in previous units). Then the ionized fraction g is computed from

$$\dot{g} = (1 - g)R \quad 2)$$

so that $n_c = g \cdot N_{v0}$.

The photon motion is numerically described on a rectangular grid either traveling with the pulse as in RAMSES or fixed around the focal volume. The latter arrangement was used to produce the movie described in Section IV.

A step ΔS is specified in the input and is $\sim 1/3 h_x$, the cell size in x , so that photons do not move more than a cell length in a time step Δt , where

$$\Delta t = \Delta S/c \quad \text{.....} \quad \text{an arbitrary definition.}$$

Details of the spatio-temporal resolution (time steps, cell size of the grid) are given in Section IV as well.

Photon motion is based on a simple predictor-corrector scheme. First we calculate the change in particle position due to the gradient in refractive index:

$$\Delta^{\ell+1/2} \tau_x = \left[\tau_y^{\ell} \left(\frac{\partial n}{\partial x} \right)^{\ell+1/2} - \tau_x^{\ell} \left(\frac{\partial n}{\partial y} \right)^{\ell+1/2} \right] \tau_y^{\ell} \Delta S$$

$$\Delta^{\ell+1/2} \tau_y = \left[\tau_y^{\ell} \left(\frac{\partial n}{\partial x} \right)^{\ell+1/2} - \tau_x^{\ell} \left(\frac{\partial n}{\partial y} \right)^{\ell+1/2} \right] \tau_x^{\ell} \Delta S$$

The variable, ℓ , denotes the value of the variable at time step ℓ . The new directions at time step $(\ell+1)$ are found to be

$$\tau_x^{\ell+1} = (\tau_x^{\ell} + \Delta^{\ell+1/2} \tau_x) \cdot D$$

$$\tau_y^{\ell+1} = (\tau_y^{\ell} + \Delta^{\ell+1/2} \tau_y) \cdot D$$

$$D \equiv 1 / [(\tau_x^{\ell} + \Delta^{\ell+1/2} \tau_x)^2 + (\tau_y^{\ell} + \Delta^{\ell+1/2} \tau_y)^2]^{\frac{1}{2}}$$

We now include the velocity straggling factor. $\Delta \vec{r} = \vec{v}_g \Delta t$ so that the updated particle positions become:

$$x^{\ell+1} = x^{\ell} + \beta(\vec{r}) \left(\frac{\tau_x^{\ell}}{2} + \frac{\tau_x^{\ell+1}}{2} \right) \Delta S$$

$$y^{\ell+1} = y^{\ell} + \beta(\vec{r}) \left(\frac{\tau_y^{\ell}}{2} + \frac{\tau_y^{\ell+1}}{2} \right) \Delta S$$

The power density in each cell is given by

$$J_{jk} = c E_{jk} / v_{jk}$$

W_{jk} = sum of all weights of the photons distributed to the cell jk by area weighting using Eq. 1 and V_{jk} is the 3-D volume of the cell. The ionization fraction is worked out by integrating Eq.

$$g^{l+\frac{1}{2}} = 1 - (1 - g^{l-\frac{1}{2}}) \exp(-R^l \Delta t)$$

All our work to date consists of attempting to simulate the break-down morphology (which we expect to be caused by beam deformation) observed by Smith et al.⁽²⁾ At the damage threshold a small number (≤ 4) micro-sites are found in NaCl. This goal dictated the particular choice of the experimental arrangement shown in Fig. 1.

In the early calculation it was established that a moving grid over a pulse is not practical. In order to improve the spatio-temporal resolution the code was modified to use a fixed rectangular grid. To save memory space, a fixed double-triangular grid over the focal volume is presently being experimented with. The resolution possible with this grid is expected to be close to resolving spatial features in the order of a few microns.

Unlike RAMSES we now have separate routines for the group velocity and refractive index. Therefore the shifting routine in RAMSES is eliminated and the code is now no longer restricted to gases but is applicable to any non-linear (or linear) pulse propagation problem where the interaction area is smaller than or equal to the $\vec{r} - t$ volume of the pulse. It is, further, a simple matter to turn "on" or "off" the interaction between matter and photons, which is equivalent to simulating classical (linear) optics.

References:

1. H. D. Düdder, D. B. Henderson, Comp. Phys. Comm. 10, 155 (1975)
2. W. L. Smith, J. H. Bechtel, N. Bloembergen, Phys. Rev. B 12, 706 (1975)
3. A. Schaid, P. Kelly, P. Brünlich, Phys. Rev. B 16, 4569 (1977)

ATE
LMED
-8